CHALMERS
UNIVERSITY OF TECHNOLOGY

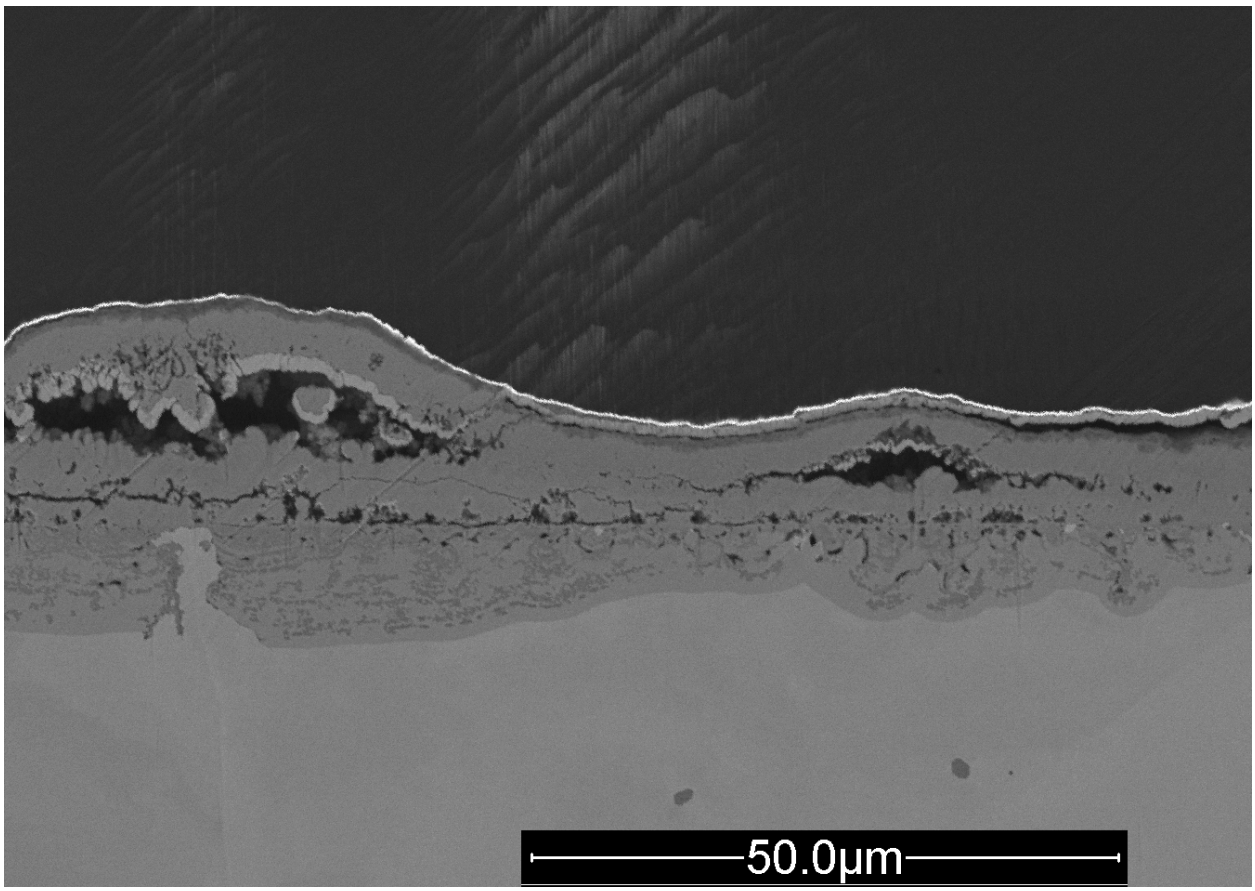

The influence of Ni on corrosion of Fe18CrXNi model alloys at 600 °C

Investigation of the oxidation after breakaway

Master's thesis in Materials Chemistry

WILLIAM FUNG

Department of Chemistry and Chemical engineering
CHALMERS UNIVERSITY OF TECHNOLOGY
Gothenburg, Sweden 2019

Master's thesis 2019

The influence of Ni on corrosion of Fe18CrXNi model alloys at 600 °C

Investigation of the oxidation after breakaway

WILLIAM FUNG

CHALMERS
UNIVERSITY OF TECHNOLOGY

Department of Chemistry and Chemical engineering
Division of Energy and Materials
Chalmers University of Technology
Gothenburg, Sweden 2019

The influence of Ni on corrosion of Fe18CrXNi model alloys at 600 °C
Investigation of the oxidation after breakaway
WILLIAM FUNG

Supervisor: Dr. Torbjörn Jonsson[a]
Supervisor: Johan Eklund[a]
Supervisor: Amanda Persdotter[a]
Examiner: Jan-Erik Svensson[a]
[a] Department of Chemistry and Chemical Engineering, Chalmers University of Technology

Master's Thesis 2019
Department of Chemistry and Chemical engineering
Division of Energy and Materials
Chalmers University of Technology
SE-412 96 Gothenburg
Telephone +46 31 772 1000

Cover: SEM image of Fe18Cr20Ni exposed in 5 % O_2 + N_2 at 600 °C for 168 hours and sprayed with K_2CO_3.

Typeset in LaTeX
Printed by [Chalmers Reproservice]
Gothenburg, Sweden 2019

The influence of Ni on corrosion of Fe18CrXNi model alloys at 600 °C
Investigation of the oxidation after breakaway
WILLIAM FUNG
Department of Chemistry and Chemical Engineering
Chalmers University of Technology

Abstract

Waste and biomass are an alternative to fossil fuel as these are CO_2 neutral and renewable as opposed to fossil fuels. However due to its content, which has substantial concentration of chlorine, alkali and water vapour it leads to a higher corrosion rate of the material used in the boilers. This results in higher costs as the material needs to be replaced more often. In fossil fuel boilers chromia forming steels are used where the formed chromia will form a protection against corrosion for the used material, but in the environment in waste and biomass-fired boilers the chromia breaks down fast. The effects of how nickel affects the oxide forming after the chromia has broken down has not been researched to the same extent as the chromia and will be investigated for this study.

The focus of this paper is to increase the understanding of the effects of nickel in a Fe18Cr-alloy. This was accomplished by conducting furnace experiments on Fe18Cr model alloys with varying nickel content. The coupons were first sprayed with K_2CO_3 to deplete the thin Cr-rich oxide and then put in a 600 °C furnace for 168 hours with an atmosphere of 5 % O_2 and N_2. The mass gain of these coupons was observed and the cross sections analysed. The cross sections were first prepared using Broad ion beam (BIB) milling and then analysed using a Scanning Electron Microscope (SEM). Chemical analysis were done using an Energy Dispersive X-ray spectroscopy (EDX) and an X-ray Diffraction (XRD).

When adding more nickel to the alloy phase transformation from ferritic to austenitic occured, resulting in slower diffusion of elements through the material. The different oxides showed regions of an inward and an outward growing oxide, where there were iron oxides and nickel oxide in the outward growing region, and a mixed spinel for the inward growing region. The results from both the TG exposures and the furnace exposures show that adding nickel is beneficial to the corrosion protective properties of an Fe18Cr alloy as the mass gain is decreased at both exposures when adding more nickel to the alloy. It is also observed that the mass gain does not change significantly after adding more than 5 % nickel. The results from the TG exposures does however show that a small decrease in mass gain is observed when the nickel content is increased.

Keywords: Fe18CrNi, secondary protection, tube furnace, thermogravimetric analysis

Acknowledgements

First and foremost I would like to thank my supervisors, Dr. Torbjörn Jonsson, PhD-student Johan Eklund and PhD-student Amanda Persdotter for making this project available and also for all the advices, help during experiments and interesting discussions.

I would also like to thank my examiner Professor Jan-Erik Svensson for the opportunity to write this thesis.

Futhermore, I would like to thank Kanthal for providing with all samples used in this project.

Finally I would like to thank everyone in the high temperature corrosion group for contributing towards an enjoyable working environment.

William Fung, Gothenburg, 09 2019

Contents

1 Introduction **1**
1.1 Aim . . . 1

2 Corrosion of metals **3**
2.1 Thermodynamic driving force . . . 3
2.2 Kinetics . . . 6
2.2.1 Linear rate law . . . 7
2.2.2 Parabolic rate law . . . 7
2.2.3 Logarithmic rate law . . . 8
2.2.4 Breakaway oxidation . . . 8
2.3 Oxide formation . . . 8
2.3.1 Diffusion through the oxide . . . 9
2.3.1.1 Lattice diffusion . . . 9
2.3.1.2 Short-circuit diffusion . . . 10
2.4 Different metal oxides . . . 11
2.4.1 Primary protection & secondary protection . . . 11
2.4.2 Iron oxides . . . 11
2.4.2.1 Hematite, Fe_2O_3 . . . 11
2.4.2.2 Magnetite, Fe_3O_4 . . . 12
2.4.2.3 Wüstite, $Fe_{1-y}O$ . . . 12
2.4.3 Chromium oxide, Cr_2O_3 . . . 12
2.4.4 Nickel oxide, NiO . . . 12
2.4.5 Mixed spinel oxides . . . 12

3 Analytical Techniques **13**
3.1 Scanning Electron Microscope (SEM) . . . 13
3.1.1 Energy Dispersive X-ray spectroscopy . . . 14
3.2 Broad ion Beam (BIB) . . . 14
3.3 X-ray Diffraction (XRD) . . . 14

4 Methods **17**
4.1 Experimental . . . 17
4.1.1 Sample preparation . . . 17
4.1.2 Removing the primary protection . . . 18
4.2 Exposures . . . 18
4.2.1 Tube furnace exposure (discontinuous) . . . 19

4.3 Thermobalance exposure (continuous) . . . 19
4.4 Broad ion beam . . . 19
4.5 Scanning Electron Microscope . . . 20
4.6 XRD . . . 20

5 Results **21**
5.1 Mass gain . . . 21
5.2 Thermogravimetric analysis . . . 22
5.3 SEM investigation . . . 24
5.4 XRD . . . 33

6 Discussion **37**
6.1 Comparison of the measured and calculated oxide thickness . . . 37
6.2 TG tests . . . 38
6.2.1 Mass gain comparison of furnace and TG exposures . . . 39

7 Conclusion **41**

8 Future works **43**

A Appendix 1 **I**
A.1 Oxidation thickness calculation . . . I
A.2 Table of mass gain from the furnace exposures . . . II

1
Introduction

The increased levels of greenhouse gases have proven to be problematic, since these has been linked to the increase of average global temperature. This has lead to a various increase of natural disasters such as heat waves, floods and hurricanes [1, 2]. One of the main greenhouse gases is CO_2 which is released during combustion of different types of fossil fuels. Because of this there is an increasing interest to replace power generating techniques which uses fossil fuels, since these produce carbon dioxide [3]. A possible replacement is waste- and biomass-fired boilers for power generation, as the fuel used in these boilers are renewable and CO_2 neutral as opposed to fossil fuel. The materials used for superheaters has traditionally been stainless steel because of its corrosion resistance as well as its mechanical properties. But the fuel in waste- and biomass-fired boilers contain more of alkali, chlorine and water vapour leading to a more corrosive environment. The materials used often contain chromium since these forms a slow-growing corundum type oxide. This type of oxide is called the primary protection of an alloy, which is very slow-growing due to the high degree of stoichiometry, resulting in low diffusion rates of ions through the oxide. In nearly all previous studies the focus has been on how to improve the primary protection, however in the very harsh environment of a waste and biomass-fired boiler the primary protection has been shown to break down. This leads to exposure of the metal, which results in a rapid formation of iron-rich oxide. This type of oxide is not as protective as chromia, but it has been shown that the growth rate of the iron-rich oxide can be influenced by changing the alloy composition. The formed iron-rich oxide can therefore be defined as the secondary protection of the alloy. The secondary protection has not been studied to the same extent as the primary protection and is not understood very well. To increase the knowledge of the secondary protection will therefore be beneficial as this could decrease the material consumption as they corrode slower. This also opens up the opportunities to design the most cost-effective secondary protection as well as the best material for the secondary protection. Therefore a study of the influence of nickel on the secondary protection is vital.

1.1 Aim

The aim of this study is to assess whether it can be beneficial or not to add nickel to an alloy and also to learn about the influence of nickel on the secondary protection as it may influence the oxides that forms when the primary protection has broken down. To test this a series of experiments has been conducted on model alloys with

varying nickel content. To observe the behaviour of the secondary protection the coupons were sprayed with K_2CO_3 on the surface. This is because the potassium in the salt will deplete the chromia which will force the alloys to transition into the secondary protection stage [4, 5].

2

Corrosion of metals

To understand why some metals have a better corrosion resistance it is important to understand the concept of corrosion and why it takes place. This chapter aims to clarify the mechanisms and the driving forces of corrosion. The main driving force of why corrosion occurs is that the metals are in a more stable state when they are oxides, and therefore will form an oxide when in contact with the oxygen in the air. This can be described using both the thermodynamics and the kinetics of the chemical reaction that occurs [6].

2.1 Thermodynamic driving force

When the metal comes in contact with oxygen it will follow reaction R 2.1 where M stands for the metal and O for the oxygen.

$$\mathrm{xM} + \frac{\mathrm{y}}{2}\mathrm{O_2} \longrightarrow \mathrm{M}_x\mathrm{O}_y \tag{R 2.1}$$

If the ionic state of the metal is more stable than the atomic state, the metal will start corroding as soon as it is in contact with the oxygen. This can be described with Gibbs free energy, where a negative ΔG indicates a spontaneous reaction and a positive value the opposite. The Gibbs free energy equation is shown in equation 2.1 [7–9].

$$\Delta\mathrm{G} = \Delta\mathrm{H} - \mathrm{T}\Delta\mathrm{S} \tag{2.1}$$

Where H is the enthalpy, S is the entropy of the reaction and T is the temperature of the reaction. The reaction entropy can be described as a measure of the degree of disorder that the product can have compared to the reactants in the reaction. If the degree of disorder is higher for the products then S will be positive for the reaction. The enthalpy of a reaction describes if the reaction requires extra energy to react or if there will be an excess of energy after the reaction. If the reaction requires extra energy to occur then H will be positive. Generally for metals is that they will form oxides in standard temperatures and pressures. Equation 2.1 can be expressed as equation 2.2 when it is expressed in terms of the reaction quotient, Q_r, which is the activity of the products divided by the activity of the reactants [7–9].

$$\Delta\mathrm{G} = \Delta\mathrm{G}^o + \mathrm{RT}\ln(\mathrm{Q_r}) \tag{2.2}$$

Where $\Delta\mathrm{G}^\mathrm{o}$ is Gibbs free energy when all reactants are in their standard states, R is the ideal gas constant and Q_r is the equilibrium constant of the reaction, which

can be described in terms of the activities of the reactants and the products [7–9]. If reaction R 2.1 and equation 2.2 are combined it equates to equation 2.3

$$\Delta G = \Delta G^{o} + RT \ln\left(\frac{a(M_xO_y)}{a(M)^x a(O_2)^{\frac{y}{2}}}\right) \tag{2.3}$$

where a is the activity of each specie. For solids the activity is approximated to be 1, when equation 2.3 reaches equilibrium ΔG equals zero and equation 2.3 can be rewritten as equation 2.4 [7–9].

$$\Delta G^{o} = -RT \ln\left(\frac{1}{a(O_2)^{\frac{y}{2}}}\right) \tag{2.4}$$

For gases the activity can also be expressed as the partial pressure of the gas, equation 2.4 can then be rewritten as equation 2.5.

$$p_{o_2} = \exp\left(\frac{\Delta G^{o}}{RT}\frac{2}{y}\right) \tag{2.5}$$

The Ellingham diagram is a representation of Gibbs free energy equation and can be used with equation 2.5 to determine what kind of oxide will form and if the metal is stable at certain temperatures [10]. An Ellingham diagram is shown in Figure 2.1.

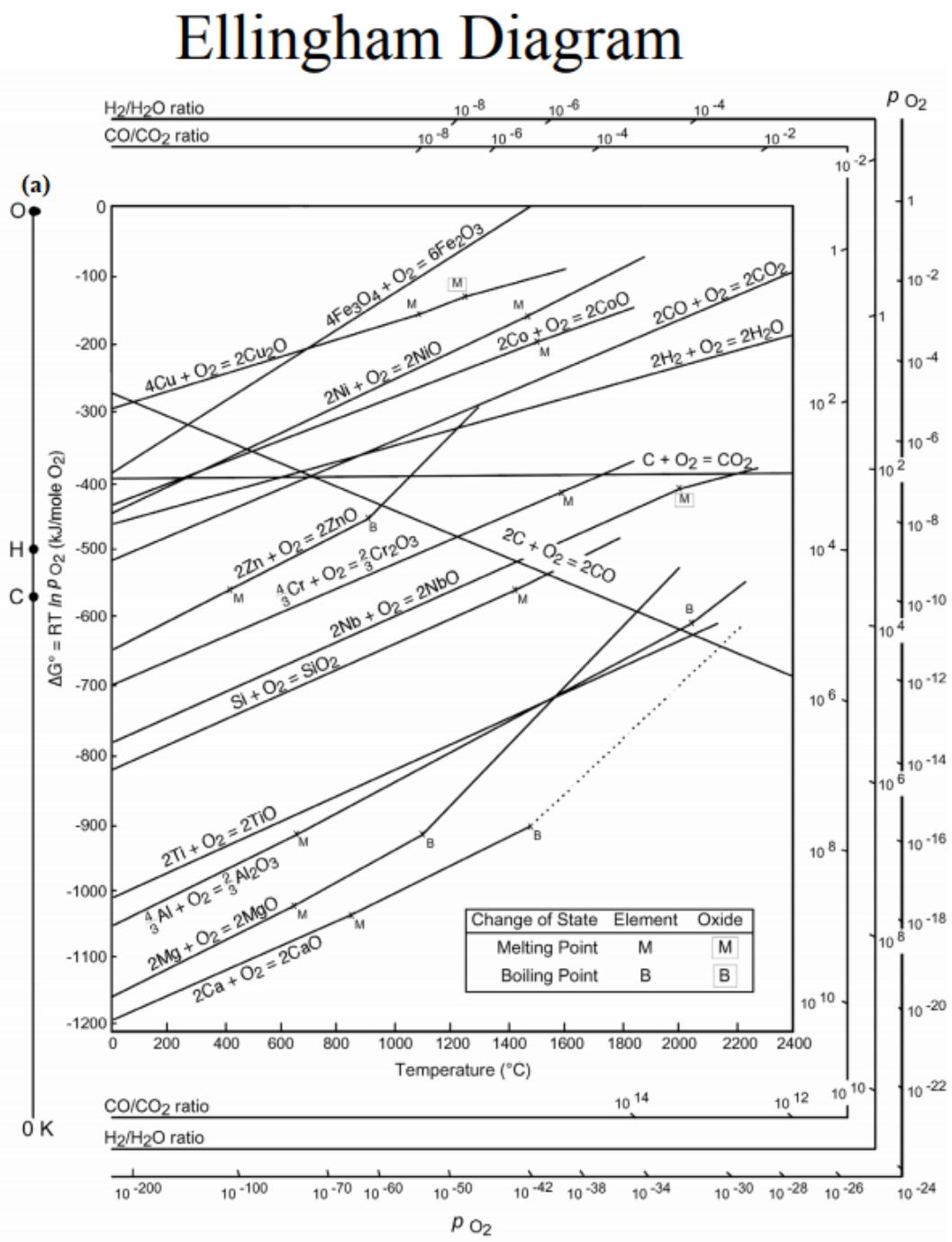

Figure 2.1: An Ellingham diagram taken from [11], showing what kind of oxides that will form for different metals with different parameters.

The Ellingham diagram is essentially a diagram where ΔG is plotted against the temperature, and because both H and S are about constant depending on the temperature the lines will be almost straight in the diagram. The diagram can be used for three purposes, the first is to determine how easy the oxides will form on the metals, the second is to determine what partial pressure of oxygen is in equilibrium with the formed oxide. It can also be used to resolve what ratio of CO/CO_2 or

H_2/H_2O is needed to reduce an oxide back to the metal. How easy the oxides will form can be observed to the left in the diagram as the more unstable metal oxides will be higher up and have a higher Gibbs free energy and be less stable. This could then be used to see which kind of metal can be used to reduce which metal oxides thermodynamically. As can be seen in Figure 2.1 most metal oxides can be reduced with the use of carbon at the right temperature. The partial pressure of oxygen of the equilibrium state for a specific reaction can be found using line (a) in the diagram, where a new line is drawn from the O-point to where a specific temperature meets a certain reaction. This line is then drawn further to partial pressure of O_2 line to determine partial pressure of O_2 at equilibrium for a reaction. This can then be used to determine if an oxide will form or not as oxides will not form when the partial pressure of oxygen is lower than that of the equilibrium. As mentioned before carbon can be used to reduce metal oxides, but depending on how stable the oxide is the reduction requires a different ratio of CO/CO_2. If the metal oxide is stable a higher amount of CO is required. How to determine what ratio is needed the same procedure as when finding the partial pressure of oxygen is followed except this time the C-point on the (a)-line will be used instead [10, 11].

2.2 Kinetics

Another factor that affects the formation of oxide is the kinetic of the oxide growth. This can be described by the help of understanding the mechanism in addition to the rate-limiting step. From reaction R 2.1 it can be observed that it is possible to analyse the oxide formation, the consumption of oxygen and the consumption of the metal. The analysis can be made with analysing the mass gain of the sample. By weighing the sample continuously the oxidation rate can be measured. There are three rate laws that are commonly used to describe the behaviour of oxides, these are are linear, logarithmic or parabolic which are all presented in Figure 2.2 [7–9]. In the figure breakaway oxidation is also presented, which is a mixture of the different rate laws.

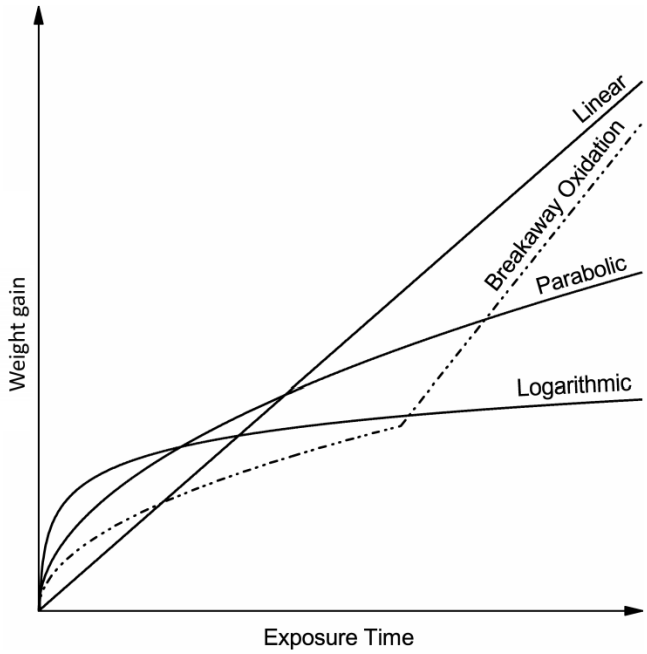

Figure 2.2: A schematic representation of the three kinetic rate laws during oxidation [12, 13].

2.2.1 Linear rate law

The oxide growth can be described with a linear rate law when the mass gain linearly depends on the time as seen in Figure 2.2. The rate law can be described with equation 2.6

$$x = k_l t + C \tag{2.6}$$

where x is the oxide thickness, k_l is the linear rate constant, t is the exposure time and C is the integration constant. This rate law mostly applies to very thin oxides or highly porous oxides, where it can be calculated as a normal reaction without any resistance. The rate-determining step is usually a phase boundary or surface process, where the adsorption of the oxygen to the oxide can be the rate-limiting step if the diffusion through the oxide is fast [7–9].

2.2.2 Parabolic rate law

At higher temperatures oxides frequently follows a parabolic rate law instead, the parabolic rate law is shown in equation 2.7

$$x^2 = k_p t + C \tag{2.7}$$

where x is the oxide thickness, t is the exposure time, C is the integration constant, but k_p is the rate constant for the parabolic rate law. The parabolic behaviour at high temperature indicates that the rate-limiting step is the diffusion, which explains the decrease in rate as the oxide layer grows thicker [7–9]. This rate law was first derived by Wagner [14] where the following statements were assumed:

- Solubility of oxygen in the metal can be ignored.
- Thermodynamic equilibrium is reached in both interfaces.
- The formed oxide layer is both dense and have good adhesion to the surface.
- The oxide has a homogeneous stoichiometry in the whole oxide [15].

2.2.3 Logarithmic rate law

At temperatures around 300-400 °C the oxide formation follows a logarithmic rate law, where the initial oxide formation is very quick followed by a stagnation of the mass gain. The logarithmic rate law can be described with equation 2.8a and equation 2.8b [15]

$$\text{Direct logarithmic } \; x = k_{log}\log(t + t_{0)} + A \tag{2.8a}$$

$$\text{Inverse logarithmic } \; \frac{1}{x} = B - k_{il}\log(t) \tag{2.8b}$$

where x is the oxide thickness, t is the exposure time, k_{log} and k_{il} is the rate constant for the direct logarithmic and the inverse logarithmic rate equations respectively and A and B are integration constants [15]. What decides why the oxide formation follows a logarithmic rate law is not entirely known. There are however some theories about it, such as rate-limiting chemisorption or rate-limiting transport of ions/electrons through the oxide [7–9].

2.2.4 Breakaway oxidation

In reality most oxides does not follow just one of the rate laws but is a mixture and their reaction behaviour can change due to several reasons such as formation of cracks or depletion of alloying elements. One of the more common mixture of rate laws is the breakaway oxidation, where the oxidation starts out following a parabolic rate law and then increases suddenly to follow a much higher rate of a parabolic rate law. This sudden increase can be caused by defects such as cracks in the protective oxide layer, which makes it easier for oxygen to diffuse to the surface thus causing it to corrode faster [7].

2.3 Oxide formation

The oxidation process of metals can be described with three steps. In the first step the oxygen from the surrounding environment adsorbs to the surface and gets reduced from the electrons from the metal. These oxygen anions then react with the metal cations and form an oxide, which will continue to grow laterally until the surface is covered. When a continuous oxide has formed the oxides will continue to grow perpendicular to the surface, but the oxidation process will slow down as the metal is no longer in direct contact with the surrounding atmosphere. The decrease in oxidation speed is due to the diffusion rate through the oxide. The process is visualised in Figure 2.3 [8].

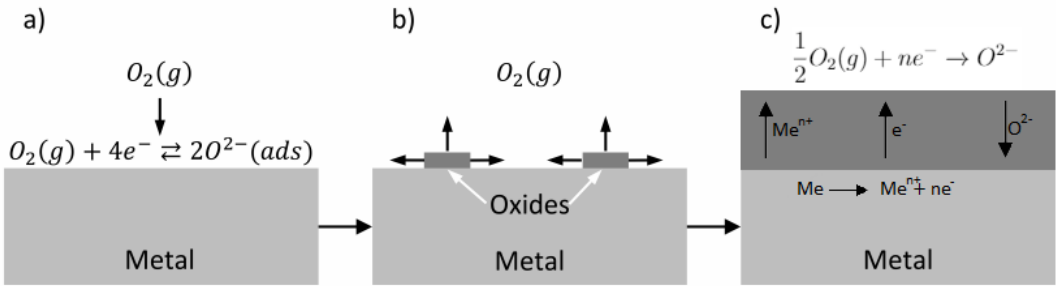

Figure 2.3: Schematic drawing of oxide formation on a metal including their reactions. The three steps are a) oxygen adsorption, b) oxide nucleation and c) continuous oxide growth. Drawing is based on [12, 13]

2.3.1 Diffusion through the oxide

Once the continuous oxide has formed the growth of the oxide depends on the diffusion of ions and electrons through the oxide. Depending on what kind of defects the oxide contains the diffusion through the oxide will behave differently. If the diffusion is through the point defects it is called lattice diffusion, if it takes faster routes through one- and two-dimensional defects such as phase boundaries and line defects in the oxide scale it is called short-circuit diffusion [16]. Both lattice and short-circuit diffusion follows equation 2.9

$$\mathrm{D} = \mathrm{D_0 e^{-\frac{Q_D}{RT}}} \tag{2.9}$$

where D is the diffusion coefficient, which is different for the two types of diffusion, $\mathrm{D_0}$ is a frequency factor, which can be approximated as temperature independent, and $\mathrm{Q_D}$ is the activation energy of the diffusion, which differs depending on the type of oxide [8].

2.3.1.1 Lattice diffusion

The rate of diffusion through the formed oxide is dependent on the defects that resides in the oxide. These defects can be divided into two groups which are point defects and line/surface defects. Defects are imperfections in the crystal lattice, point defects as the name suggests are defects in a single point in the lattice. There are several point defects and the Frenkel and Schottky defects are the more relevant ones regarding corrosion [8]. Frenkel defects are when ions in the lattice moves in between other atoms in the lattice, creating both an interstitial and a vacancy. Schottky defects are when ions leaves the lattice and creates a vacancy, this causes a counter ion to also leave to balance the charges [8, 17].

These defects creates vacancies that enable ion transport through the oxide, but they do not enable electron transport. The electron transport can be explained with non-stoichiometric oxides. These non-stoichiometric oxides are also called semiconductors where they can be divided into two groups, p-type and n-type. The p-type

has positive electron holes as a result of either metal vacancies or oxygen interstitials. The n-type is the opposite with metal ion interstitials or oxygen deficiency, which results in positive charges which are balanced by an excess of electrons. These two types of defects explain the mechanism of how the electrons can be transported. The line and surface defects contains various types of defects. One of the types are along the grain boundaries, where the grain boundary is irregular, which causes impurities to segregate along the grain boundary. Other types can be voids and cracks in the oxide scale [8, 18, 19]. Lattice diffusion is diffusion through these said point defects, which are presented in Figure 2.4.

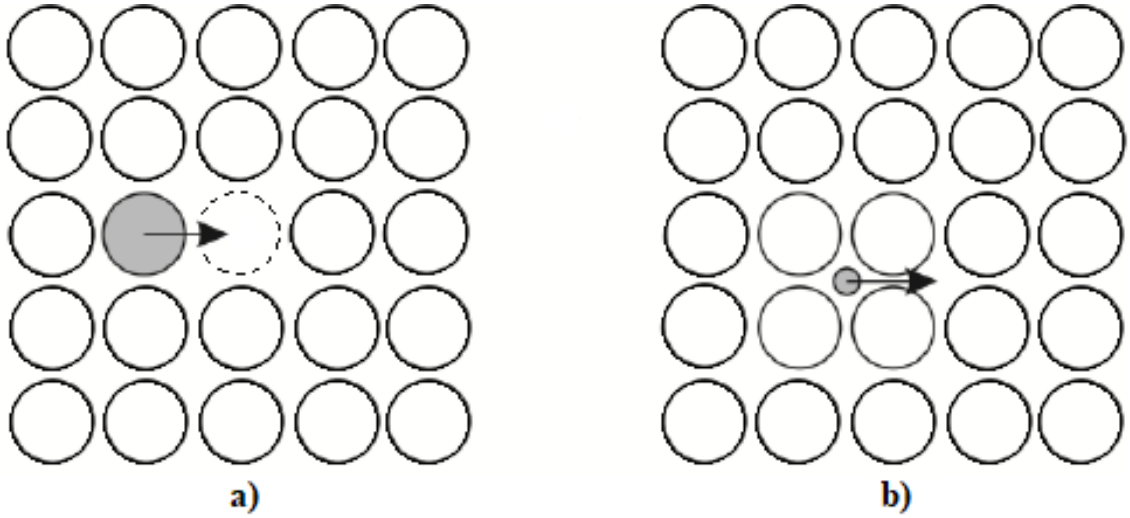

Figure 2.4: Schematic drawing of the main mechanism of lattice diffusion. a) vacancy diffusion and b) interstitial diffusion. Illustration based on [20].

The vacancy diffusion occurs in the presence of at least one vacancy in the lattice where one atom or ion travels from its lattice position to a vacancy, which creates a new vacancy. The interstitial diffusion is where one interstitial atom or ion moves to another vacant interstitial site [8].

2.3.1.2 Short-circuit diffusion

Short-circuit diffusion is transport through the oxide without migrating through the oxide lattice, but rather through other diffusion paths that are faster. The different paths can be grain boundaries or other defects that occur during oxide growth such as line dislocations. This kind of diffusion is more relevant at lower temperatures (<600 °C) where the lattice diffusion is much slower, increasing the impact of the flux of atoms along the grain boundaries. At higher temperatures the lattice diffusion is more important, but this also depends on various factors such as concentration of defects and size of the grains [8, 16].

2.4 Different metal oxides

There are many various metal oxides that can be formed and the thermodynamic driving force predicts if certain metal oxides will form. One thing that decides if the oxide is a protective layer against corrosion or not is the diffusion kinetics of the oxide. If the diffusion of ions through the oxide is slow then the oxide has passivity and is therefore a protective layer since the corrosion will be slow. How this works is that even though the formed oxide layer is very thin the diffusion rate through it is extremely slow, which results in the oxide acting as a barrier that separates the metal from its environment [21].

2.4.1 Primary protection & secondary protection

The primary protection usually consists of a thin and slow growing oxide layer that covers the whole alloy, which prevents the alloy from oxidizing further. The secondary protection is the oxide that forms after the primary protection broken and usually grows at a higher rate, which makes it less protective. The primary protection of alloys containing chromium is chromium oxide, which is both slow growing and protective. When sprayed with K_2CO_3 the chromium layer will deplete and the secondary protection of iron oxide will form, this depletion follows reaction R 2.2 [4].

$$Cr_2O_3\,(s) + 2\,K_2CO_3\,(s) + \frac{3}{2}\,O_2\,(g) \longrightarrow 2\,K_2CrO_4\,(s) + 2\,CO_2(g) \qquad (R\,2.2)$$

Depletion of the chromia also happens when in contact with water following reaction R 2.3 [5].

$$\frac{1}{2}Cr_2O_3\,(s) + \frac{3}{4}O_2\,(g) + H_2O\,(g) \longrightarrow CrO_2(OH)_2(g) \qquad (R\,2.3)$$

2.4.2 Iron oxides

At temperature >570 °C there are three possible iron oxides that can form, which are hematite, magnetite and wüstite. All three of them have different crystal structure, hematite has a corundum structure, magnetite an inverse spinel structure and wüstite a rock salt structure [8, 22].

2.4.2.1 Hematite, Fe_2O_3

Hematite has a corundum crystal structure that consists of hexagonal closed packed oxygen ions with metal ions filling up $\frac{2}{3}$ of the central octahedral sites. Compared to the other iron oxides, hematite has the highest stoichiometry which also results in a small diffusion coefficient. This makes the iron oxide have a slow oxide growth and is in that sense the most protective of the iron oxides. As hematite is oxygen deficient at temperatures 650-800 °C it behaves as an n-type semiconductor, but shows p-type behaviour at higher temperatures [8, 23].

2.4.2.2 Magnetite, Fe_3O_4

Magnetite has an inverse spinel crystal structure, where the oxygen ions are cubic close packed and the metal ions are split between the octahedral and tetrahedral sites. The split between the sites depends on the valency of the metal, where the divalent ions will occupy the tetrahedral sites and the trivalent will go to the octahedral sites. Since iron can be both divalent and trivalent, magnetite is considered an inverse spinel, which is when half of the divalent ions will occupy the octahedral sites instead. Magnetite has a metal deficiency at higher oxygen partial pressure and oxygen excess at a lower oxygen partial pressure, therefore it behaves as a p-type semiconductor [8, 24].

2.4.2.3 Wüstite, $Fe_{1-y}O$

With the chemical composition $Fe_{1-y}O$ it can be seen that wüstite has a oxygen deficiency and is therefore a p-type semiconductor. The oxide has a high degree of nonstoichiometry which results in a big diffusion coefficient. This also makes the oxide have a rapid growth, resulting in a thick oxide at higher temperatures [8, 25].

2.4.3 Chromium oxide, Cr_2O_3

There are different chromium oxides that can form, but the only stable form of chromium oxide at higher temperatures is Cr_2O_3. Just as hematite it has a corundum structure where the Cr ions occupy $\frac{2}{3}$ of the octahedral sites. In similarity to hematite chromium oxide also has a very high stoichiometry, giving it very slow oxide growth even at higher temperatures. Measurements on chromium oxides has shown that it behaves like an n-type semiconductor at low oxygen partial pressure and shifts to p-type when at elevated oxygen partial pressure. This suggests that it is dependent on how close to the surface the oxide is, as it would get a higher oxygen partial pressure closer to the surface [8, 26].

2.4.4 Nickel oxide, NiO

Nickel oxide has a rock salt structure with both nickel and oxygen at the octahedral sites. When exposed at high temperatures in presence of water it has shown a parabolic behaviour and also some voids in the metal/oxide interface [27].

2.4.5 Mixed spinel oxides

Mixed spinel oxides are oxides that follow a general formula of $M^{2+}M_2^{3+}O_4$, where there are two cations with different charge combined with oxygen atoms. The M^{2+} cations occupy the tetrahedral sites while the M^{3+} cations occupy the octahedral sites and the oxygen ions are cubic close packed. Inverse spinels can also occur where the formula is $M^{3+}(M^{2+}M^{3+})O_4$, this occurs when half of the M^{2+} and M^{3+} switch place [28].

3
Analytical Techniques

For a better understanding of the behaviour of the secondary protection it is vital to analyse the exposed coupons. The first step in the analysis was to analyse the mass gain of each coupon after exposure. These coupons was further analysed with several other analysis methods to get other pieces of information about the samples. These pieces of information can then be used to expand the knowledge of the secondary protection. The analysis methods that was used are Thermogravimetic Analysis, Scanning Electon Microscope, Energy Dispersive X-ray spectroscopy and X-ray Diffraction. The purpose of this chapter is to describe the said techniques to give a more clear picture of the obtained results.

3.1 Scanning Electron Microscope (SEM)

SEM is a very powerful analysis method as it has a high spatial resolution and a large depth of field. The technique utilises an electron beam to generate signals that can be used to analyse the samples. There is a lot of information that can be obtained from SEM, e.g. the topography, the chemical composition and microstructure of the sample. The SEM can be divided into three parts, an electron column where the electrons are focused and accelerated, a sample chamber and at least one type of detector for the electrons [29].

Some limitations of SEM is that it requires vacuum and that the samples has to be both solid, conductive and small enough to fit in the sample chamber. The quality of the electron gun determines how good resolution the SEM will have. To obtain good imaging the probe size should be as small as possible while the velocity of the electrons should be as high as possible. However a high velocity would give a worse resolution for backscattered electrons since it gets a higher interaction volume. The interaction volume is the volume that the used electrons penetrates into the sample. The sputtered electrons from the electron gun have a lot of kinetic energy which will have different interactions with the sample, where different information can be obtained depending on which type electron is detected [29].

The most common electrons that are used for imaging are the secondary(SE) and the backscattered electrons(BSE). The backscattered electrons are high energy electrons which upon contact with the sample will go around nuclei and back from the sample. This gives information about the contrast in the composition of the sample. The contrast is due to the different attractive forces of the nuclei, a heavier atom will

have a more attractive nucleus. Some of the electrons may not interact with nuclei and instead will interact with the electrons where they will repel an electron out from the sample, these are called the secondary electrons. However some of these only lose parts of its initial energy and still backscatter out of the sample, making the backscattered imaging less trustworthy. The secondary electrons will give information of both topography and morphology, it can create a 3D-like picture because of the edge-effect where more electrons leaves the sample at edges and therefore creates a brighter spot in the SEM image. The 3D-like picture is also due to the detector that are positioned on the side of the sample. The other signals that can be detected are X-rays, visible light, heat and backscattered diffracted electrons. The characteristic X-rays can then be used for an Energy Dispersive X-ray spectroscopy, EDX [29].

3.1.1 Energy Dispersive X-ray spectroscopy

The X-rays that are scattered out from the sample can be detected by a specific detector which gives information about chemical composition. How the information is obtained is that by launching electrons onto the sample will eject other electrons from the sample, which leaves vacancies that can be filled by electrons from higher energy states. When these vacancies are filled the electrons that fills them emit X-ray radiation, which have characteristic energies depending on which element it is. The information that is obtained is both qualitative and quantitative. The signals from the analysis are characteristic for the elements that are detected and the strength of the signals are correspondent to the quantity of the elements [30].

3.2 Broad ion Beam (BIB)

Ion beam techniques have a variety of uses, it can be used for patterning, metal deposition and also to obtain information about the sample. The information that can be obtained is imaging of the topography and cross section of the sample. The ion beam techniques are all based on the same principle where heavy ions, for example gallium or argon, are sputtered onto the surface. By changing the energy the ions are sputtered with, the application is different. The different applications ranges from gentle polishing of the surfaces to removing material quickly. The technique used in this paper is broad ion beam, which has a broad beam up to 2 mm and was used to obtain high quality cross sections [31, 32].

3.3 X-ray Diffraction (XRD)

XRD is a non-destructive analysing method which is based on the scattering of X-rays. It uses Bragg's law which is shown in equation 3.1. When the scattered X-rays are in phase they can either give a destructive or a constructive interference.

$$n\lambda = 2d \sin \theta \tag{3.1}$$

In equation 3.1 n stands for the order of reflection and is always a positive integer, λ is the wavelength of the incoming photons, d is the space between two atomic planes and θ is the angle of reflection. All of the variables are measured with XRD except for the spacing between the planes which can therefore be calculated through Bragg's law. This can then be compared to a database with all the characteristic intensities and the crystalline phase can be determined. The acquired intensity peaks will also enable qualitative analyses for determining the lattice constant and it can further be used to obtain the particle size and the crystallization degree. To perform an X-ray diffraction a source of X-rays is required along with a sample holder and a detector that is connected to a computer [33].

4
Methods

4.1 Experimental

4.1.1 Sample preparation

The Fe18CrNi alloys with the desired composition were received from Kanthal. The received alloys were cut down to sizes of ~10.8 x 10.8 x 1.9 mm and a hole with 1.5 mm in diameter was added to the coupon for easier handling. This resulted in a total surface area of ~3.1 mm^2. The composition of the coupons that were tested is listed in Table 4.1.

Table 4.1: Content, microstructure and substrate grain size of the alloys received from Kanthal.

		Content of the alloys				
Test	**Alloys**	**Fe (wt%)**	**Cr (wt%)**	**Ni (wt%)**	**Microstructure**	**Substrate grain size (μm)**
Ref.	Fe18Cr	Bal.	18	0	100 % ferrite	150
1	Fe18Cr	Bal.	18	0	100 % ferrite	150
2	Fe18Cr2Ni	Bal.	18	2	100 % ferrite	90
3	Fe18Cr5Ni	Bal.	18	5	90 % ferrite	8
4	Fe18Cr10Ni	Bal.	18	10	50 % ferrite	60
5	Fe18Cr20Ni	Bal.	18	20	Austenite	60
6	Fe18Cr34Ni	Bal.	18	34	Austenite	70
7	18Cr82Ni	0	18	82	Austenite	110

A schematic picture of the coupon is shown in Figure 4.1. First the short sides, a-d in the figure, were polished with a Silicon Carbide Grinding Paper, Grit 1000. It was polished until the surface was completely even and there were no visible scratches. When the side surfaces were done the top and bottom surface, e-f in the figure, were polished using a Struers Tegrapol-31 with a Tegra Force 5 following Table 4.2. The grinding times, grinding paper and liquid can all be found in Table 4.2.

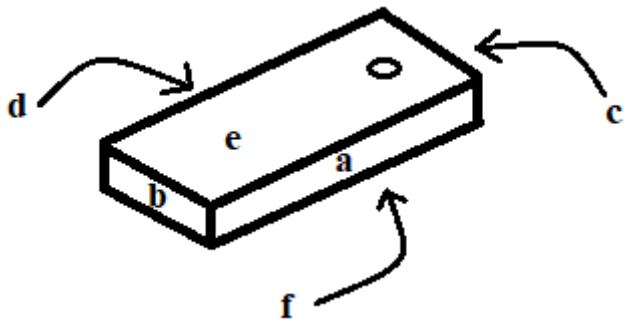

Figure 4.1: Schematic picture of a coupon with letters explaining which sides are described.

Table 4.2: Grinding times and used grinding paper for the coupons.

Grind number	Grinding time [s]	Grinding paper	Grinding liquid
1	40	Silicon carbide grinding paper grit 500	Distilled water
2	40	Silicon carbide grinding paper grit 1000	Distilled water
3	35	Silicon carbide grinding paper grit 2400	Distilled water
4	35	Silicon carbide grinding paper grit 4000	Distilled water
5	30	MD-Dac	Diamond suspension, 3 µm
6	25	MD-Nap	Diamond suspension, 1 µm

After polishing the coupons achieved a mirror-like surface and were transferred into a tube that was filled with acetone and then sealed. The tube was put in an elmasonic P to be cleaned using ultrasound for 20 minutes at 50 °C, 37 kHz and power 100. When the ultrasound was finished the coupons were transferred into plastic sample holders that were first cleaned with ethanol. The coupons were kept in the plastic holders, which was placed in a dessicator, until moved to the furnace exposure.

4.1.2 Removing the primary protection

The coupons were spray coated with K_2CO_3 until a concentration of 1 ± 0.1 mg/mm^2 was reached. Why K_2CO_3 was chosen is because it destroys the primary protection of chromium hence allowing the secondary protection to form. The depletion of the primary protection follows reaction R 2.2.

4.2 Exposures

First a reference test was conducted over 24 hours on the Fe18Cr and then compared to old results to remove any uncertainties caused by the operator. When the results

were satisfactory the longer exposures could begin.

4.2.1 Tube furnace exposure (discontinuous)

The sprayed coupons exposed in furnaces for 168 hours at a temperature of 600 °C and with an atmosphere of 5 % O_2 + bal. N_2. All different alloys were tested in groups of three to eliminate any outliers and achieve a more precise statistical value. The data are then processed to show the average result and also the positive and negative deviation from the average value.

4.3 Thermobalance exposure (continuous)

In addition to the mass gain that is observed from the 168 hours exposure a Thermogravimetric Analysis, TGA, was conducted to better understand the oxidation kinetics. In the TGA for this project the samples are exposed to heat in an atmosphere of 5 % O_2 + bal. N_2 and the mass of each sample is monitored continuously. There are two different modes in TGA, one of which the mass change is plotted against the temperature change, while the other is isotherm and plots time against the mass change [34]. The one that was used in this study is the isothermic one. The samples of this study was ramped up and then exposed to 600 °C, therefore the interesting information from the TGA was the oxidation kinetics and how the alloys behaves at 600 °C [34]. From the TGA data it is also possible to get the incubation time of the oxides, which in our case is when the primary protective oxide breaks and the secondary protection forms. The TGA typically consists of a high precision scale and a temperature programmable furnace, which is also connected to a computer that can track the results continuously.

4.4 Broad ion beam

In order to analyse the oxide with SEM the coupons were cut and ion milled to analyse the sample cross section. Before cutting, the coupons were sputtered with a layer of either palladium or gold using a Emitech K550X, this was in order to better observe the sample in the SEM. Eventual damage to the oxide could be observed in the SEM as the palladium/gold would show up as very bright and any crack in the image would indicate damage to the oxide. The parameters for the sputtering was a coating current of 25 mA, a coating time of 3 min and rotating samples. After sputtering, a silica wafer was glued on to the coupon with Loctite 415 and dried for 24 hours. When this procedure was done the coupons could be cut using a Struers Minitom spinning at 250 rpm. Then these cross sections were refined using a broad ion beam, BIB, where argon ions are sputtered onto the sample. The used BIB was a Leica Tic 3X with an accelerating voltage of 8 kV, a sputtering current of 3 mA and a running time of 5 hours.

4.5 Scanning Electron Microscope

To check if the cross sections from the BIB was good enough a FEI Quanta 200 FEG ESEM was used. In the SEM the cross section of the oxide was observed for cracks and other defects such as scratches. If those did not show up it was determined that the cross section was good. Pictures of the cross sections were saved with different magnifications starting with 200x, 400x, 800x, 1600x and 3000x. The image from the 3000x magnification was then used for an EDX analysis where the different layers were characterized. The EDX was also used to check the chemical composition of the given samples to ensure the right samples were given and to ensure the rest of the EDX data. If the oxide layer was thin a LEO Ultra 55 was used instead as it has a higher resolution in addition to a possiblity for a lower working distance with the used detectors.

4.6 XRD

The samples that remained after the SEM analysis of the cross section was used for an XRD analysis. The XRD analysis was used in order to confirm the different oxides in the samples. However as magnetite has the same crystal structure as spinel the two are hard to separate in an XRD analysis. The coupons were analysed and then the XRD result was matched with a database where the most plausible oxides that matched with the results were chosen.

5
Results

5.1 Mass gain

After 168 hours of exposure at 600 °C the coupons were weighed and the mass gain was recorded. The mass gain is presented with its minimum and maximum values in Figure 5.1(see Table A.1 in Appendix A.2).

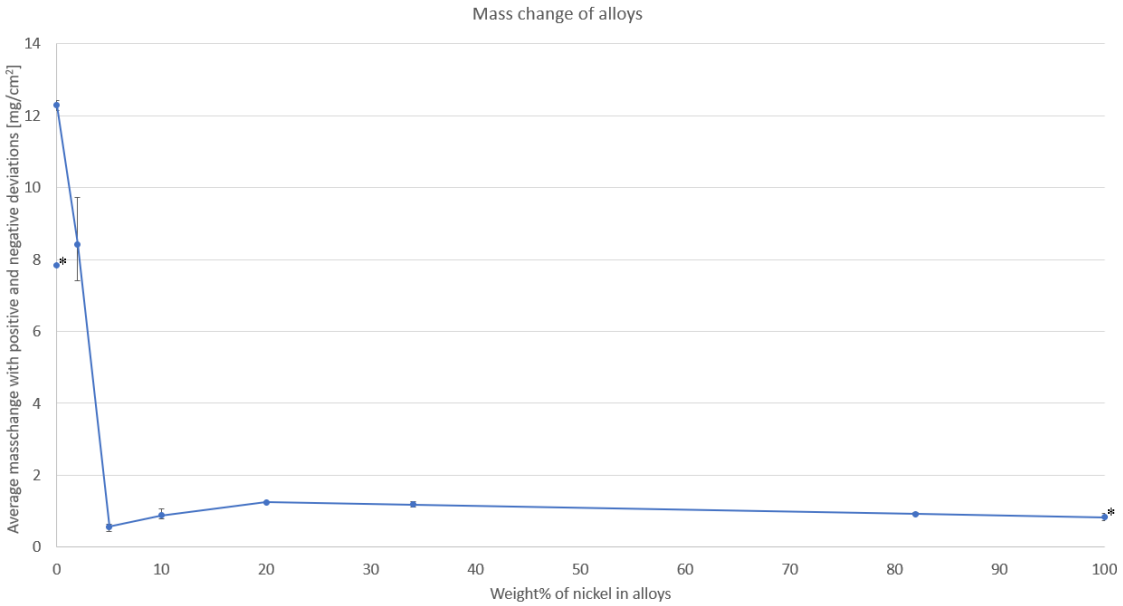

Figure 5.1: Graph of mass gain with different alloys exposed in 5 % O_2 + bal. N_2 and sprayed with 1 mg/cm^2 K_2CO_3 and their respective maximum and minimum values from the average. The asterisk is from data taken from [27] for the pure nickel and from [5] for the Fe18Cr where the atmosphere was 5 % O_2 40 % H_2O and bal. N_2 and the sample was not sprayed with K_2CO_3 and H_2O acts as the corrosive agent.

It can be observed that the mass gain decreases significantly at 5Ni, but stays relatively constant for the samples with a higher Ni content. The error bars for the samples with higher than 5 % nickel are barely visible, which indicates a small spread in test results. The Fe18Cr2Ni sample has a higher maximum and minimum value from the average mass gain compared to the other samples. It can also be observed that the samples from the other studies that were not sprayed with K_2CO_3 and exposed to water had a lower mass gain. With the mass gains known it was possible

to calculate the thicknesses of the oxides using A.1. The calculated thicknesses are presented in table 5.1.

Table 5.1: Average calculated thickness of each alloy exposed in 5 % O_2 + bal. N_2 and sprayed with 1 mg/cm^2 K_2CO_3. The asterisk is from data taken from [27] for the pure nickel and from [5] for the Fe18Cr where the atmosphere was 5 % O_2 40 % H_2O and bal. N_2 and the sample was not sprayed with K_2CO_3 and H_2O acts as the corrosive agent.

Alloys	**Avg. calculated thickness (μm)**
Fe18Cr*	54.900
Fe18Cr	85.992
Fe18Cr2Ni	58.944
Fe18Cr5Ni	3.985
Fe18Cr10Ni	6.198
Fe18Cr20Ni	8.766
Fe18Cr34Ni	8.288
18Cr82Ni	5.086
100Ni*	2.000

The calculations are made with the assumptions that the oxides are completely uniform, compact and that only one type of oxide forms.

5.2 Thermogravimetric analysis

The TG data in Figure 5.2 shows the oxidation kinetics of the alloys. It can be observed that both the Fe18Cr and the Fe18Cr2Ni displayed a very low mass gain for ~4 hours, which indicates that it was able to retain a thin and protective oxide for ~4 hours. The samples get a sudden increase in mass gain at around 4 hours which is continued throughout the rest of the exposure, reaching a mass gain of 12.9 mg for Fe18Cr and a mass gain of ~14.7 mg for Fe18Cr2Ni. The Fe18Cr5Ni sample follows a similar trend, but the low mass gain is retained for ~18 hours and then increasing, reaching a mass gain of ~1.9 mg. The samples with 10-82 weight% Ni follows the same mass gain trend, where the mass gain immediately gets a minor increase, which then increases very slightly throughout the rest of the expousre. The FeCr10Ni sample reached a mass gain of ~1.6 mg, the Fe18Cr20Ni a mass gain of ~0.86 mg, the Fe18Cr34Ni a mass gain of ~0.69 mg and the 18Cr82Ni a mass gain of ~0.22 mg. For the alloys with 5 % or more nickel, the mass gain decreases slightly with increasing concentration of nickel.

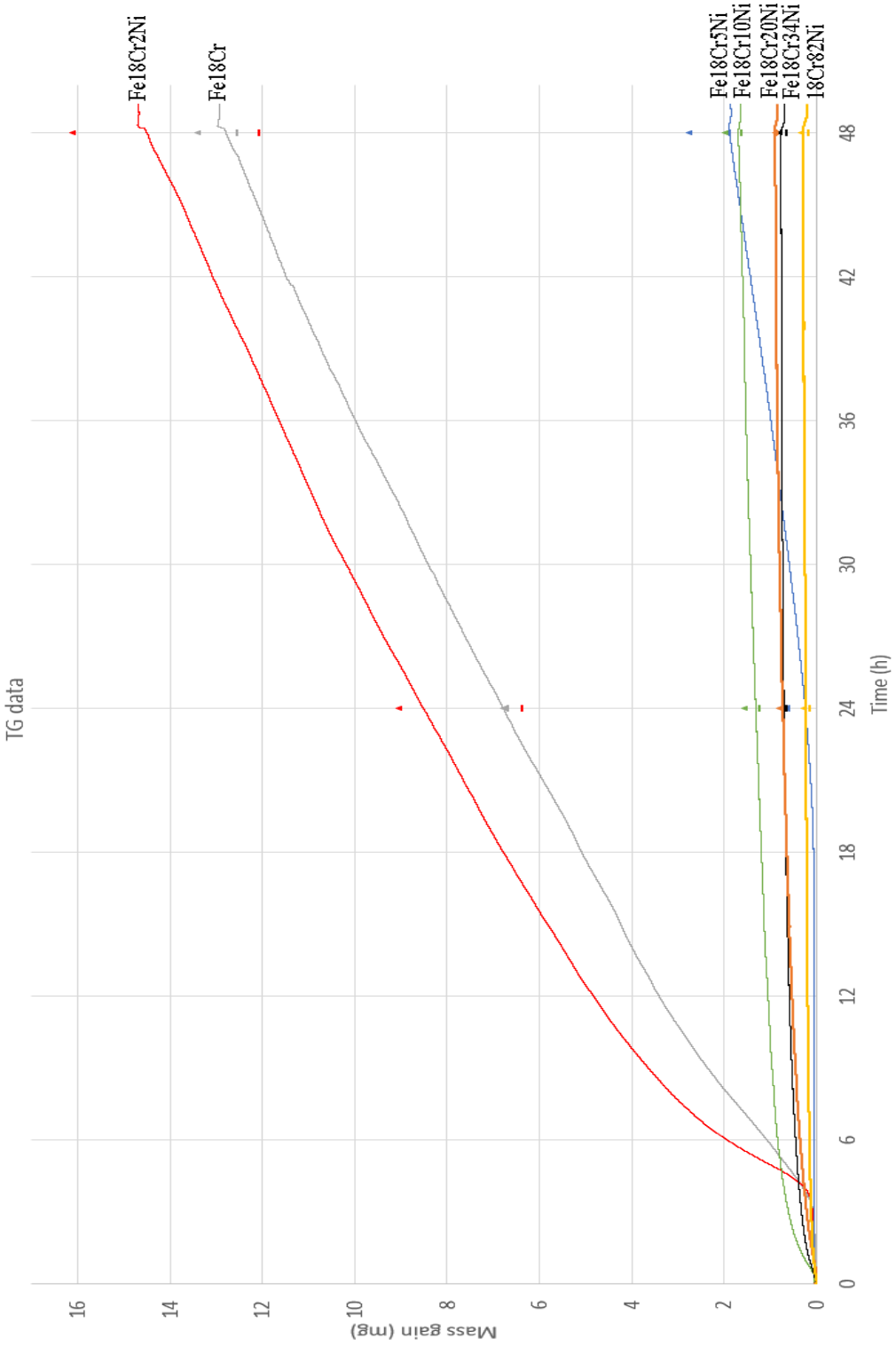

Figure 5.2: The most average TGplot of each alloy with its positive (Δ) and negative(-) deviations. The asterisk for the negative deviation of the Fe18Cr2Ni test is to denote that particular test was ran for 72 hours instead of 48 hours.

The incubation times until breakaway for all model alloys are obtained from the TG data and presented in Table 5.2. The Fe18Cr and Fe18Cr2Ni alloys both have around 4 hours incubation time, while the alloys with more than 10 weight% Ni all have a incubation time close to 0. The Fe18Cr5Ni sample has the longest incubation time of ~18 hours.

Table 5.2: Approximate incubation times for the different oxides.

Alloys	**Incubation time (hours)**
Fe18Cr	3.6
Fe18Cr2Ni	4
Fe18Cr5Ni	18
Fe18Cr10Ni	0.5
Fe18Cr20Ni	0.5
Fe18Cr34Ni	0.1
Fe18Cr82Ni	0.3

5.3 SEM investigation

The SEM images of the oxides formed on different alloys after 168 hours exposure in 5 % O_2 + bal. N_2 and sprayed with 1 mg/cm^2 K_2CO_3 is presented in Figure 5.3-5.10. EDX analysis was conducted on the alloys where the composition of the alloys were confirmed. The EDX analysis was further used to review the content of the oxide where the inward and outward growing oxides have different concentrations of the alloying elements.

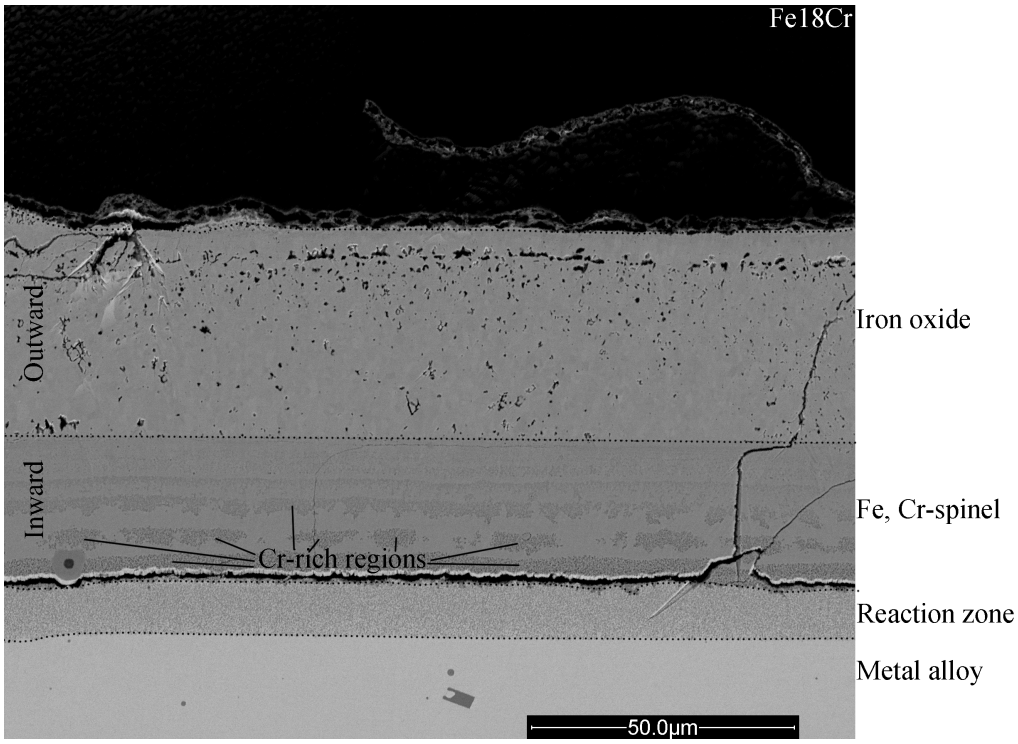

Figure 5.3: SEM-BSE image of the cross section of Fe18Cr after exposure in 5 % O_2 + bal. N_2 and sprayed with 1 mg/cm^2 K_2CO_3 at 600 °C for 168 hours.

From Figure 5.3 it can be seen that the oxide grown on the Fe18Cr sample is rather thick (~70 µm) with an inward and an outward growing oxide marked in the figure. The outward growing oxide of ~40 µm has two layers, these can be assumed to be hematite and magnetite, with hematite on top since it is more thermodynamically stable at higher oxygen partial pressure. The cations of the inward growing oxide, which is ~30 µm, is an Fe(~45-59 atomic%), Cr(~41-55 atomic%)-spinel, whereas ~57% of the spinel consists of oxygen. The spinel structure is assumed based on the data from the EDX analysis and a layer of potassium carbonate is assumed to be on top of the sample since it was sprayed on before the exposure. The darker spots in the inward growing region are more chromium rich. The composition of the layers are from data taken from EDX. Below the oxide a reaction zone is observed which is where the internal oxidation takes place and the alloy is only partially oxidised [35].

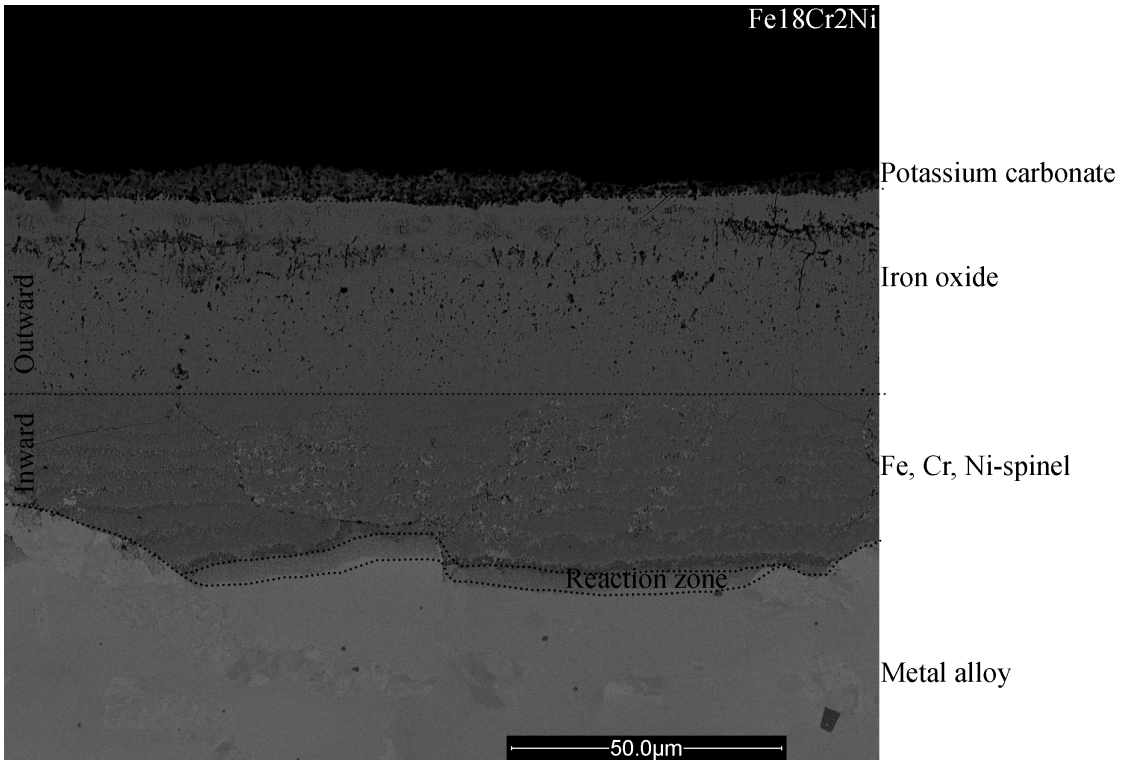

Figure 5.4: SEM-BSE image of the cross section of Fe18Cr2Ni after exposure in 5 % O_2 + bal. N_2 and sprayed with 1 mg/cm^2 K_2CO_3 at 600 °C for 168 hours.

The oxide grown on the Fe18Cr2Ni alloy is 59-73 µm thick with average thickness of ~68 µm. In Figure 5.4 an inward growing oxide of ~30 µm, an outward growing oxide of ~38 µm and a reaction zone can be observed. The outward growing oxide is split in two layers, where it can be assumed that the layers are hematite and magnetite with hematite on top. The cations of the inward growing oxide is an Fe(~57-58 atomic%), Cr(~38-40 atomic%), Ni(~2-4 atomic%)-spinel. These assumptions are made from the observations of the data from both the EDX and the XRD analyses. On top of the oxide a layer of potassium carbonate is observed, which is confirmed using the XRD analysis.

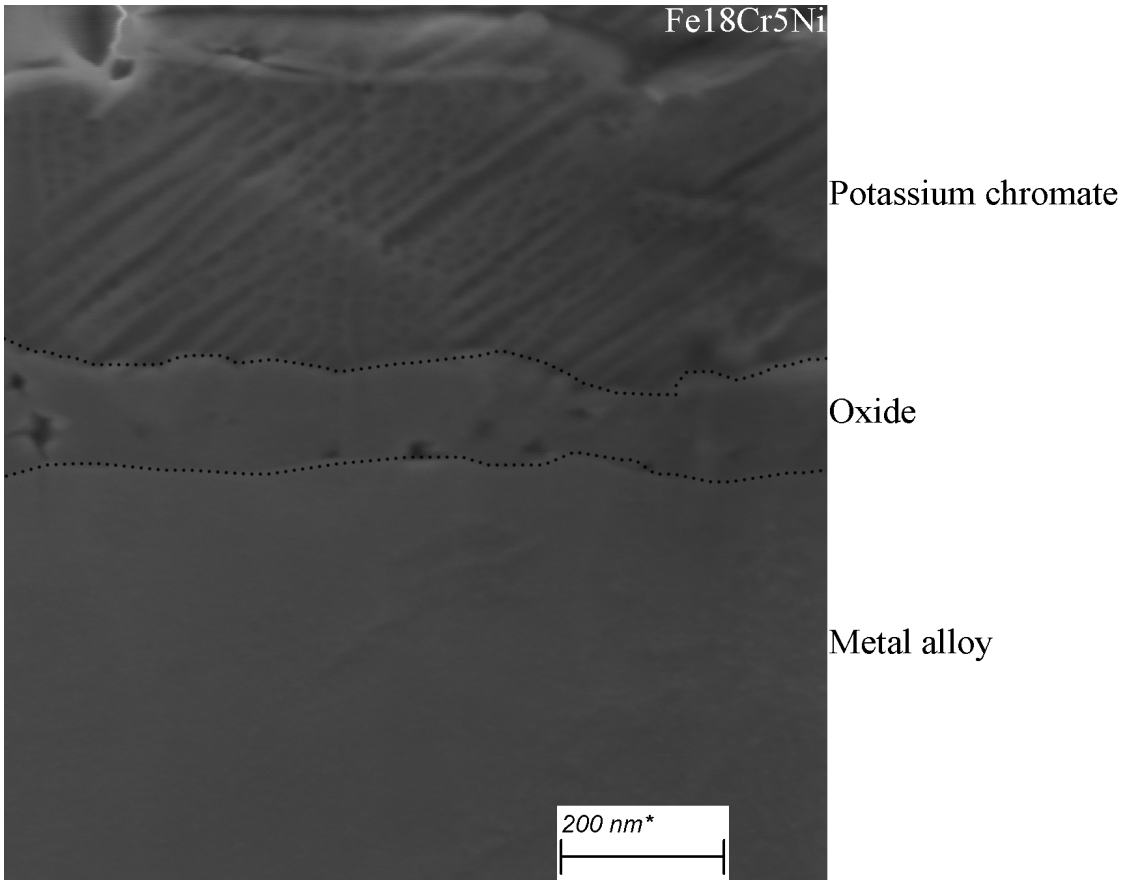

Figure 5.5: Ultra SEM-SE image of the cross section of Fe18Cr5Ni after exposure in 5 % O_2 + bal. N_2 and sprayed with 1 mg/cm^2 K_2CO_3 at 600 °C for 168 hours.

The oxide from the Fe18Cr5Ni was ~120 nm, which is too thin for the ESEM and therefore an LEO Ultra 55 SEM was used instead as it has higher resolution, see Figure 5.5. The oxide grown on the Fe18Cr5Ni alloy is very thin and therefore an inward or outward growing oxide cannot be confirmed. The EDX analysis of the oxide showed a composition of 43-60 atomic% of Fe, 26-38 atomic% of Cr, 1-2 atomic% of Ni and 12-18 atomic% of K. The potassium found in the analysis is from the sprayed layer of K_2CO_3 which shows that the interaction volume is larger than the area of the oxide. The XRD analysis confirmed that potassium chromate had formed, which we assume to be on top of the oxide. An EDX mapping of the sample was also performed which is presented in Figure 5.6.

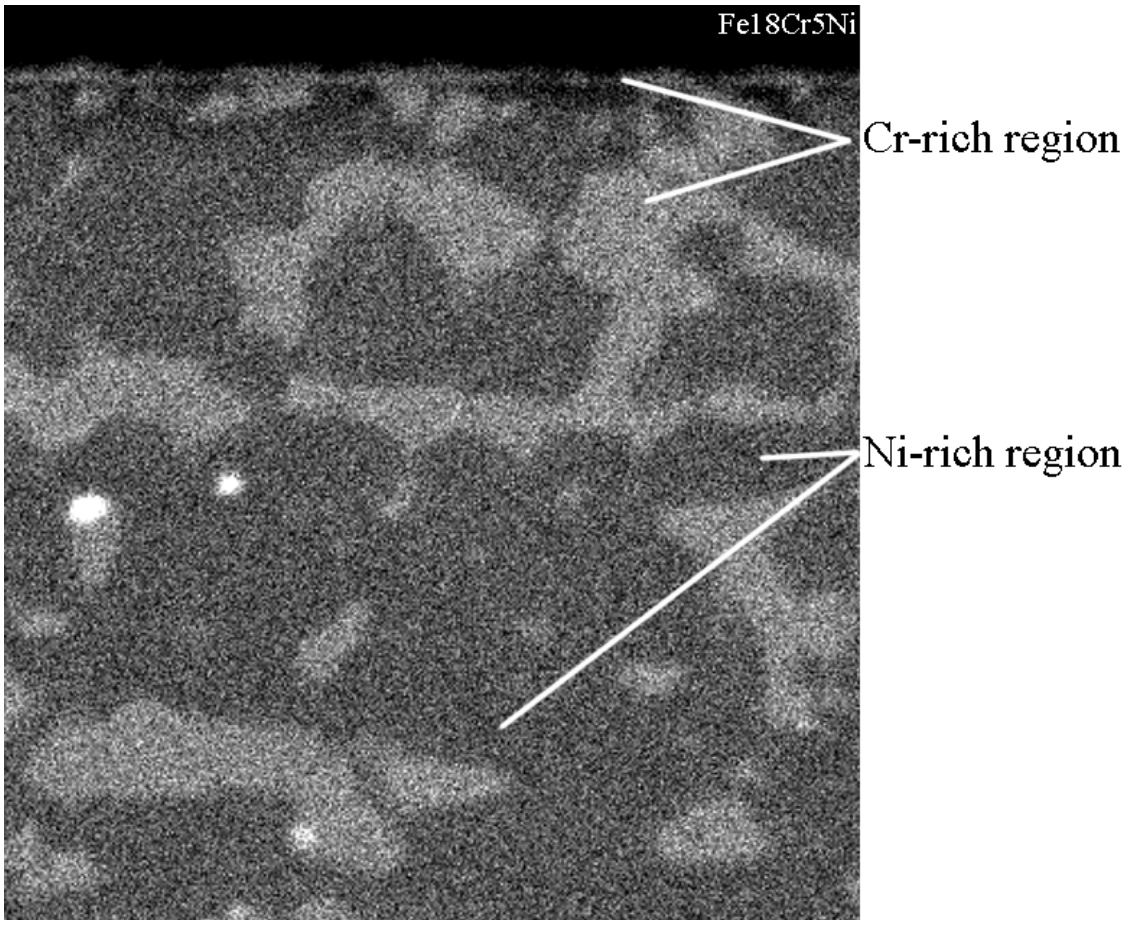

Figure 5.6: EDX mapping of Cr of the Fe18Cr5Ni sample after exposure in 5 % O_2 + bal. N_2 and sprayed with 1 mg/cm^2 K_2CO_3 at 600 °C for 168 hours.

Figure 5.6 is a mapping of the cross section of the Fe18Cr5Ni alloy where the bright areas indicate higher concentrations of Cr (22 weight%) and the darker areas indicate lower concentrations of Cr (18 weight%), while the white spots indicate chromium carbides with 62-81 atomic% chromium. Figure 5.6 in addition to the XRD results confirms an expected duplex behaviour of the Fe18Cr5Ni sample where both austenitic and ferritic(Cr-rich) parts could be found.

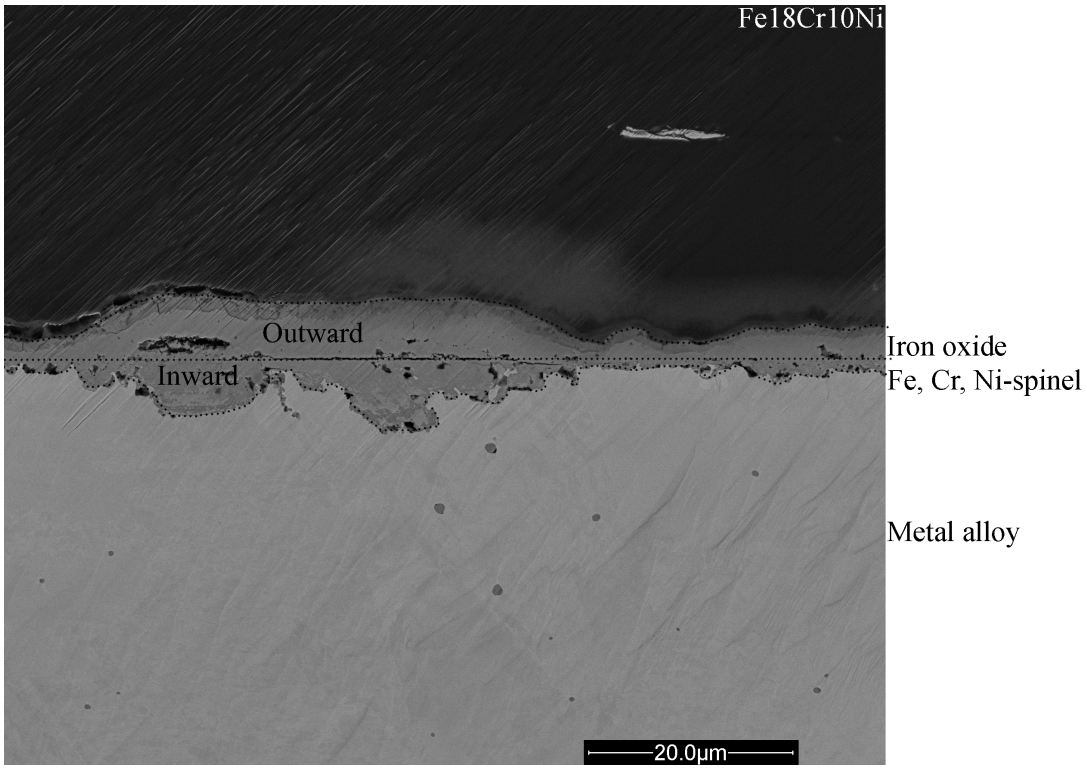

Figure 5.7: SEM-BSE image of the cross section of Fe18Cr10Ni after exposure in 5 % O_2 + bal. N_2 and sprayed with 1 mg/cm^2 K_2CO_3 at 600 °C for 168 hours.

The Fe18Cr10Ni oxide is ~8.8 µm but less uniform compared to the previous oxides, but an inward growing oxide of ~1-7 µm and an outward growing oxide ~2-6 µm is still present. The inward growing oxide can be divided into three different thicknesses, ~1 µm thick which covers ~34 % of the oxide, ~3-6 µm thick which covers ~52 % of the oxide and ~7 µm which covers ~14 % of the oxide. The outward growing oxide is ~82 % covered with ~5-6 µm thick regions while the remaining ~18 % have a thickness around 2-4 µm. The regions in the Fe18Cr10Ni sample consists of iron oxide in the outward growing region with two layers and the cations of the inward growing oxide consists of an Fe(~42-59 atomic%), Cr(~28-50 atomic%), Ni(~7-13 atomic%)-spinel. The atomic percentages in the spinel is recalculated to exclude the oxygen, as the oxygen was not excluded in the EDX quantification. These assumptions are made from observations of the data from the EDX analysis. The outward growing oxide also contains two different layers where the top layer is thinner, which is assumed to be hematite and magnetite with hematite on the top. A layer of potassium carbonate is assumed above the oxide since it was sprayed on before the exposure. The reaction zone is not apparent in the SEM image of the Fe18Cr10Ni sample.

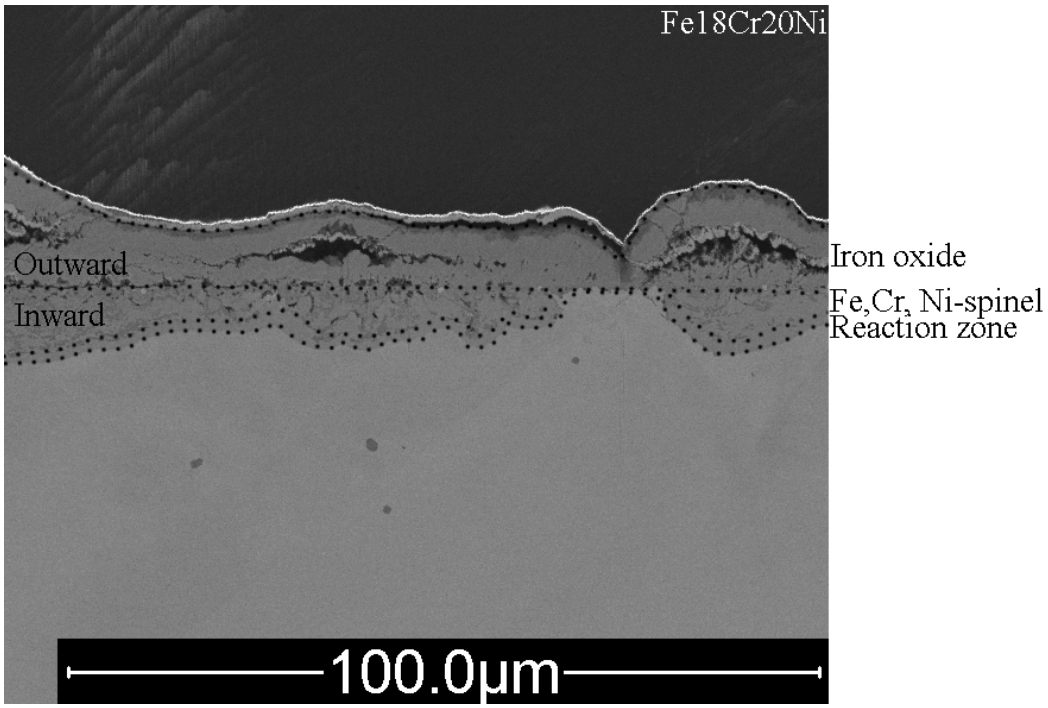

Figure 5.8: SEM-BSE image of the cross section of Fe18Cr20Ni after exposure in 5 % O_2 + bal. N_2 and sprayed with 1 mg/cm^2 K_2CO_3 at 600 °C for 168 hours.

The Fe18Cr20Ni oxide is ~17.3 µm thick has an outward growing iron oxide(~5-13 µm) and an inward growing oxide(~1-9 µm) consisting of Fe(~36-39 atomic%), Cr(~31-37 atomic%), Ni(~25-33 atomic%)-spinel, when counting the cations. These assumptions are made from observations of the data from the EDX analysis. The atomic percentages in the spinel is recalculated to exclude the oxygen, as the oxygen was not excluded in the EDX quantification. The outward growing oxide shows two layers and has a large pore and the reaction zone is visible at the bottom of the inward growing oxide. Both regions with similar pores as in the middle of the outward growing oxide and regions with a very thin inward growing oxide, similar to the right side in Figure 5.8 could be found throughout the whole oxide.

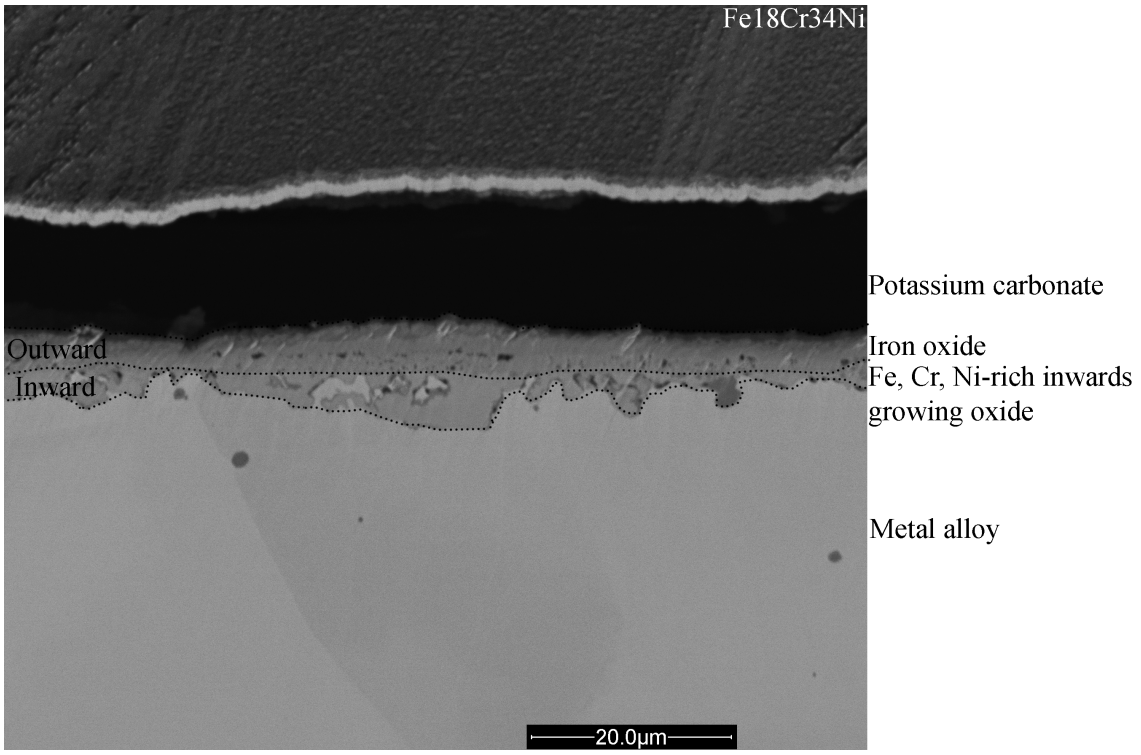

Figure 5.9: SEM-BSE image of the cross section of Fe18Cr34Ni after exposure in 5 % O_2 + bal. N_2 and sprayed with 1 mg/cm^2 K_2CO_3 at 600 °C for 168 hours.

The oxide grown on the sample with 34 % Ni is ~6.8 µm thick with the outward growing oxide~3-5 µm thick and inward growing oxide ~1-5 µm thick, both clearly visible in Figure 5.9. It can be observed that the outward growing oxide is iron oxide and divided into two layers distinguished by the difference in contrast. The two layers are interpreted as magnetite and hematite, probably with hematite on top as hematite is more stable at higher partial oxygen pressure. The inward growing oxide consists of Fe(~15-18 atomic%), Cr(~27-33 atomic%), Ni(~49-58 atomic%), when counting the cations. From the XRD analysis a layer of potassium carbonate is also found, which is assumed to be on top of the oxide. All the assumptions are made from observations made from data from the EDX and the XRD analyses.

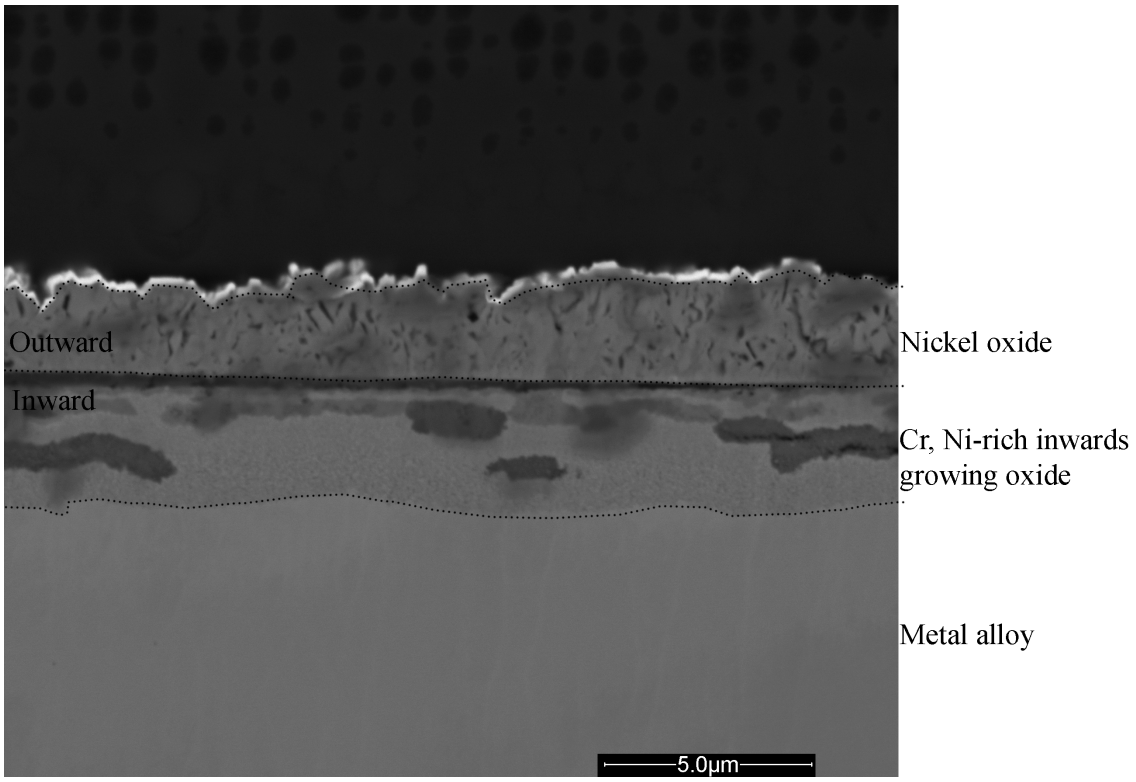

Figure 5.10: SEM-BSE image of the cross section of 18Cr82Ni after exposure in 5 % O_2 + bal. N_2 and sprayed with 1 mg/cm^2 K_2CO_3 at 600 °C for 168 hours.

In absence of iron in the sample the 18Cr82Ni instead formed a nickel oxide in the outward growing oxide(~1-3 µm) and a oxide consisting of Cr(~26 atomic%), Ni(~74 atomic%) in the brighter parts in the inward growing oxide(~3-4 µm), the whole oxide is ~5.5 µm. The darker spots in the inward growing oxide were not analysed. These assumptions are made from observations of the data from the EDX analysis. The atomic percentages in the spinel is recalculated to exclude the oxygen, as the oxygen was not excluded in the EDX quantification. There is no visible reaction zone.

The measured thicknesses of the oxides from the SEM images are presented in Table 5.3.

Table 5.3: Measured oxide thickness of each alloy from the SEM images.

Alloys	**Avg. measured thickness (µm)**	**Standard deviation (µm)**
Fe18Cr	69.8	± 3.7
Fe18Cr2Ni	68.4	± 6.6
Fe18Cr5Ni	0.12	± 0.04
Fe18Cr10Ni	8.8	± 5.9
Fe18Cr20Ni	17.3	± 7.1
Fe18Cr34Ni	6.8	± 3.9
Fe18Cr82Ni	5.5	± 0.3

To obtain the values in Table 5.3 the thinnest and the thickest thickness was measured to get a thickness that could represent the whole oxide. It can be seen that the thickness is significantly lower at the oxides with 5-82 % Ni. The Fe18Cr20Ni sample had pores and the oxide was not uniform and therefore got a higher value. The different portions between inward and outward growing oxide is presented in Table 5.4

Table 5.4: The portions of inward and outward growing oxide for the alloys.

Alloys	**Part outward growing oxide (%)**	**Part inward growing oxide (%)**
Fe18Cr	60	40
Fe18Cr2Ni	52-64	36-48
Fe18Cr5Ni	-	-
Fe18Cr10Ni	48-67	33-52
Fe18Cr20Ni	42-62	38-58
Fe18Cr34Ni	48-58	42-52
Fe18Cr82Ni	35-38	62-65

From table 5.4 it can be observed that oxides starts at a 60/40-split between outward and inward growing oxide for the Fe18Cr and the Fe18Cr2Ni. For the samples with 10-34 % Ni the split is closer to 50/50 and for the 18Cr82Ni the split is closer to 40/60 for outward and inward growing oxide.

5.4 XRD

The only coupons that remained for the XRD analysis were Fe18Cr2Ni, Fe18Cr5Ni and Fe18Cr34Ni. The XRD results of said samples are presented in Figure 5.11-5.13.

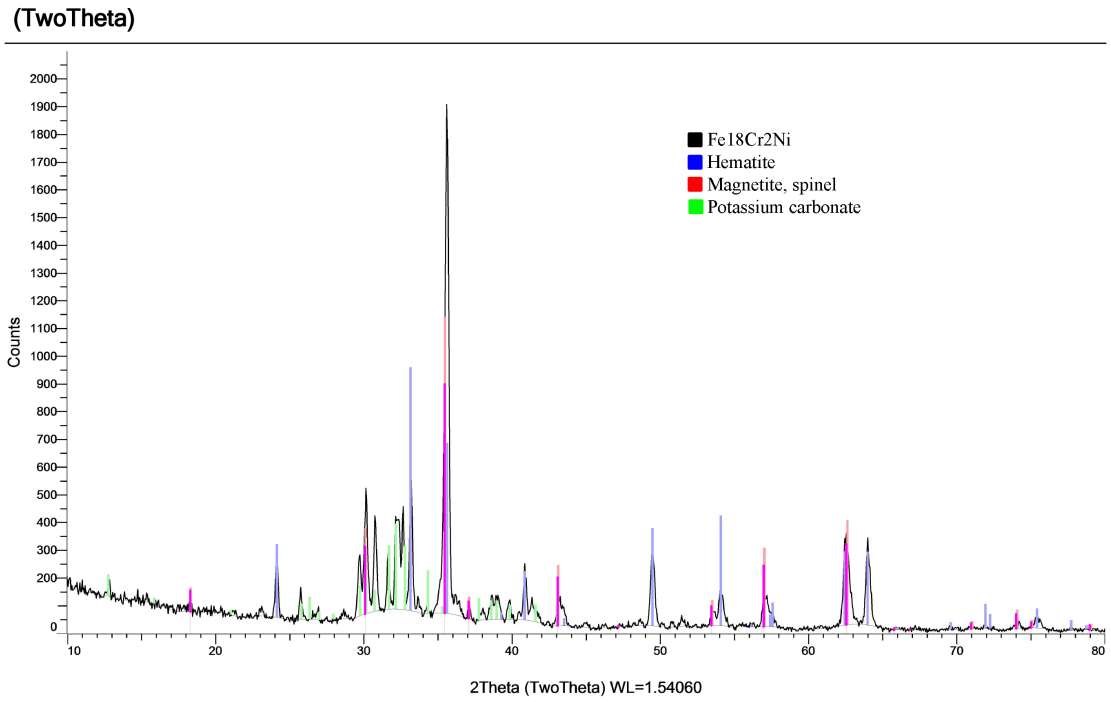

Figure 5.11: XRD diffractogram of the Fe18Cr2Ni coupon after exposure in 5 % O_2 + bal. N_2 and sprayed with 1 mg/cm^2 K_2CO_3 at 600 °C for 168 hours, showing the possible existing oxides. The diffractogram for Fe18Cr2Ni shows good matching with hematite, magnetite and K_2CO_3. The pink lines are from a combination of both hematite and magnetite.

With the results from the XRD analysis shown in Figure 5.11, the two layers in the outward growing region from Figure 5.4 can be confirmed to be hematite and most likely magnetite. It is uncertain if the red lines are signals from the magnetite or from the Fe, Cr, Ni-spinel since both have the same crystal structure and gives the same signals in XRD.

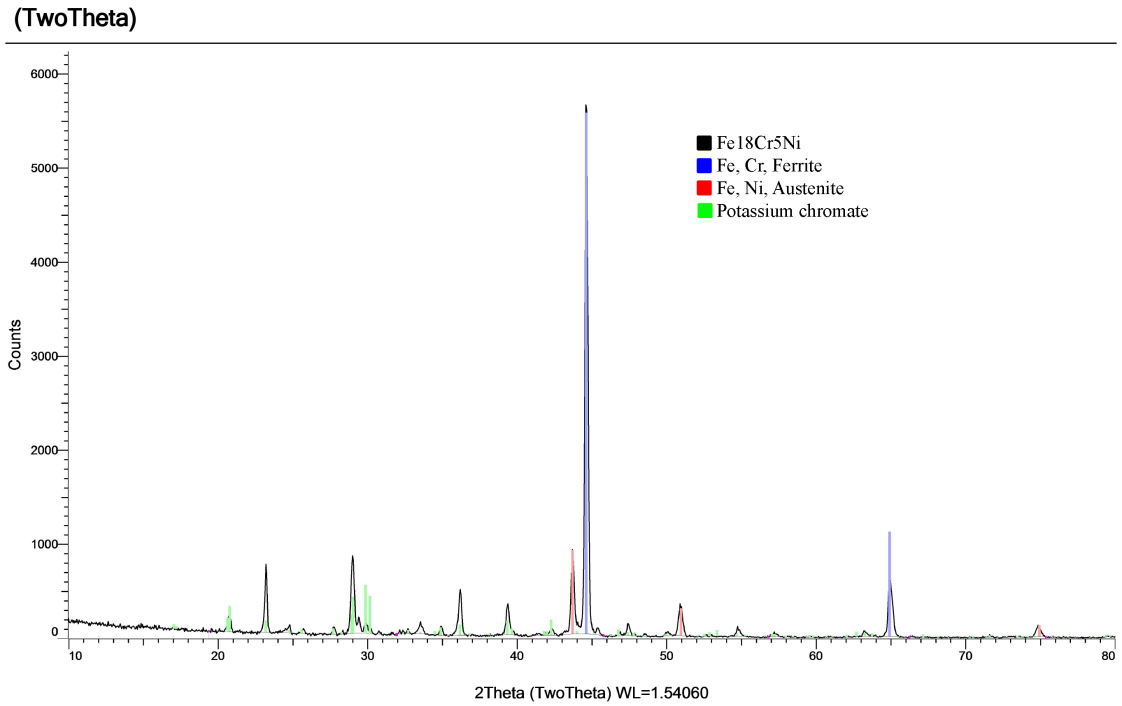

Figure 5.12: XRD diffractogram of the Fe18Cr5Ni couponafter exposure in 5 % O_2 + bal. N_2 and sprayed with 1 mg/cm^2 K_2CO_3 at 600 °C for 168 hours, showing the possible existing oxide layers. In the 5Ni coupon ferrite, austenite and K_2CO_3 are found.

The XRD analysis of the Fe18Cr5Ni sample shows that ferrite and austenite are present in the sample, which are both present in the bulk. The results are however hard to use to confirm any layers in the oxide since it is too thin for the used angle and time in the XRD analysis.

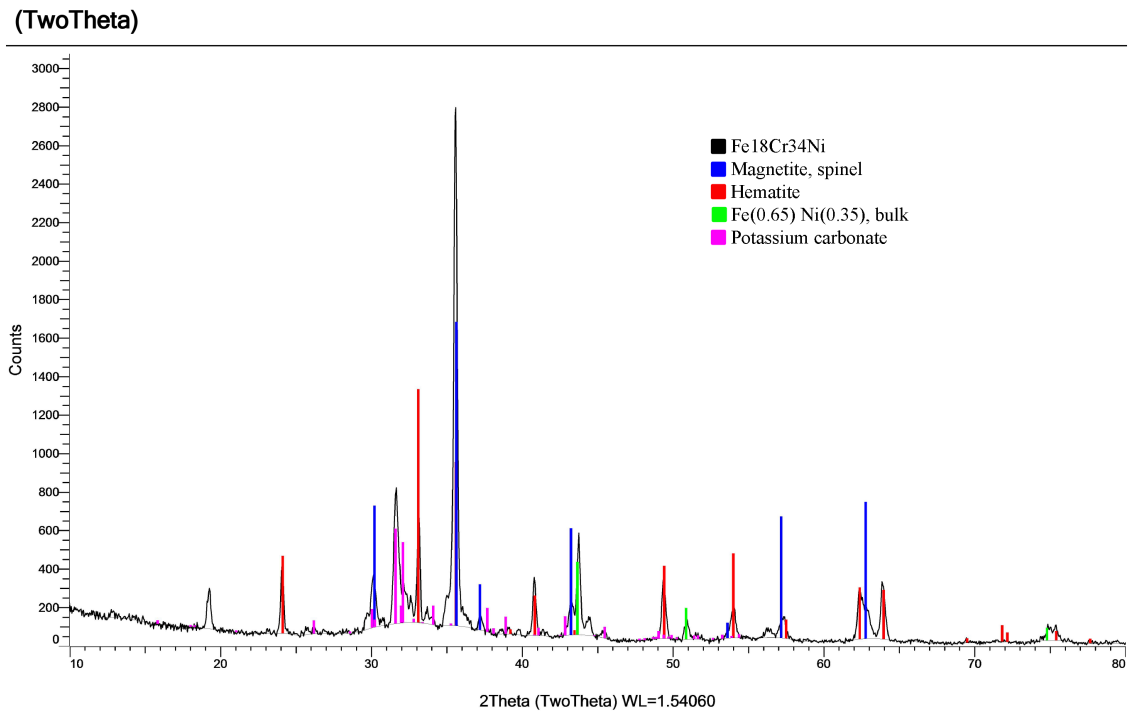

Figure 5.13: XRD diffractogram of the Fe18Cr34Ni coupon after exposure in 5 % O_2 + bal. N_2 and sprayed with 1 mg/cm^2 K_2CO_3 at 600 °C for 168 hours, showing the possible existing oxide layers. In the 34Ni coupon chromite, hematite, the bulk and K_2CO_3 are found.

The XRD results show that the 34Ni sample has both hematite and magnetite/spinel. The XRD confirms the hematite layer in the outward growing region in Figure 5.9. It is uncertain if the blue lines are signals from the magnetite or from the spinel since both have the same crystal structure and gives the same signals in XRD.

6
Discussion

6.1 Comparison of the measured and calculated oxide thickness

With the mass gain of each sample known the oxide thickness can be calculated using equations in Appendix A.1. Where the F value, molar mass % of oxygen in the metal oxide, of magnetite, Fe_3O_4, was calculated to 27.6 % and the ρ_{recalc} to 1.43 g/cm^3. The calculated thicknesses are shown in Table 5.1. For the alloys without iron NiO, nickel(II) oxide, was used instead to calculate the oxide thickness, where the F value was 27.3 % and the ρ_{recalc} to 1.82 g/cm^3. When comparing the results of Table 5.1 and table 5.3 a difference in oxide thickness can be observed, these two tables are summed up in table 6.1.

Table 6.1: Comparison of table 5.1 and table 5.3. The difference is calculated with the average measured thickness.

	Average thickness (μm)		**Difference**	
Alloys	**Calculated**	**Measured**	**Length (μm)**	**Percent (%)**
Fe18Cr	85.6	65.1 - 72.6	16.8	12.2
Fe18Cr2Ni	58.9	56.5 - 69.4	-4.1	-3.2
Fe18C5Ni	4	0.16 - 0.79	3.5	370.2
Fe18Cr10Ni	6.2	2 - 13	-1.3	-8.7
Fe18Cr20Ni	8.8	3 - 24.2	-4.8	-17.6
Fe18Cr34Ni	8.3	2.9 - 10.7	1.5	11.0
18Cr82Ni	5.1	4.7 - 5.7	-0.1	-1.0

There is no notable trend between the difference in mass gain between the calculated and the measured oxide thickness for the different alloys, but the difference could be explained by that the calculations are made with respect to only one iron oxide/nickel oxide. Since the calculations of the iron oxides were made with respect to magnetite the measured oxides should be thinner than the calculated ones. This decrease in thickness can be explained by hematite forming, which has both a higher density and a higher oxygen density compared to magnetite. The calculations also assume a perfectly uniform and compact oxide. This is however not what is happening as some oxides had varying thickness throughout the whole sample and can therefore be an explanation of why the real results differ from the expected results. The comparison of the measured and the calculated thicknesses shows that

the uneven oxide thickness is not the only explanation for difference as the uneven oxides does not result in a bigger difference. The oxides does follow the same trend regarding to oxide thickness in comparison to the nickel content, as the thickness is significantly decreased at 5 % nickel and then stays relatively unchanged at higher nickel content. The thicker measured thickness of the Fe18Cr20Ni sample could be explained by the cracks that were apparent in the whole oxide as these were included in the calculation of the measured thickness. The cracks would also allow oxygen to come in contact with alloy which would make the measured oxide even thicker. Another large deviation from the other results is the measured thickness of ~0.16-0.79 µm of the Fe18Cr5Ni sample, as the primary protection was still intact the mass gain has to come from something other than oxide formation. The sample was however not analysed using a plan-view SEM, to see if the primary protection was intact on the whole sample. The mass gain from the sample could have depended on the potassium chromate that had formed or from possible breaks of the primary protection of the sample.

6.2 TG tests

The TG exposures showed that the oxidation kinetics was not linearly dependent (see Figure 5.2), therefore a parabolic behaviour was tested since a parabolic behaviour is common for oxide growth where the diffusion is the rate-limiting step. As the parabolic rate law follows equation 2.7 the mass gain squared was plotted against time, instead of the weight against time. If the sample follows a parabolic behaviour, then the mass gain squared against time plot will be linear. The results show that only the Fe18Cr10Ni and the 18Cr82Ni alloys exhibited a slight parabolic behaviour. This could be an effect of the 48 hours exposure as it could be too short for the samples to reach a parabolic behaviour.
The behaviour of the samples in the TG exposures can be explained by the microstructures of the alloys, where adding more nickel to a Fe18Cr alloy will make it go from ferritic to austenitic. In the EDX mapping shown in Figure 5.6 the Fe18Cr5Ni alloy showed a duplex behaviour, with a Cr-rich ferritic layer near the top. From the EDX quantification it showed that the Cr-rich layer had 22 weight% of chromium instead of the 18 weight% the alloy should have, which would make the primary protection break down at a later stage, which is also apparent in the TG exposure. In the TG exposure the Fe18Cr and the Fe18Cr2Ni, which are ferritic, samples starts at a very low mass gain, which indicates that a primary protection of chromium oxide has formed. The mass gain then suddenly starts increasing after 4 hours of exposure, which indicates breaking of the primary protection. The Fe18Cr10Ni-18Cr82Ni are close to or fully austenitic where the diffusion of Cr is slow, this results in chromia not forming and an immediate mass gain as is shown in the TG exposure in Figure 5.2. The samples Fe18Cr10Ni-18Cr82Ni shows a decreasing mass gain trend with an increase of Ni in the sample. This could indicate that adding nickel is beneficial for the secondary protection, as the primary protection has depleted for those samples.

6.2.1 Mass gain comparison of furnace and TG exposures

When comparing the mass gain of the samples from the 168 hours furnace exposures and the 48 hours TG exposures it is noted that the mass gain trend is different. This is shown in Figure 6.1.

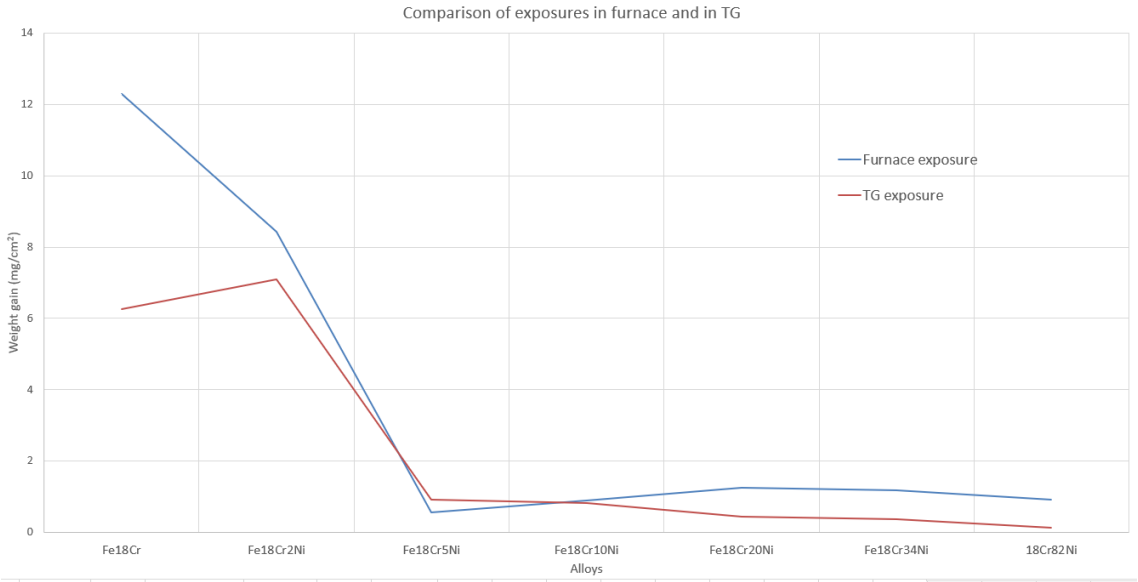

Figure 6.1: Comparison of mass gain from samples exposed in 600 °C and 5 % O_2 + bal. N_2O for 168 hours in a furnace and 48 hours in a TG.

For the furnace exposures the Fe18Cr5Ni sample had the lowest mass gain and for the TG exposures the 18Cr82Ni sample had the lowest mass gain. This could be explained by the difference in air flow. Both of the exposures has the same atmosphere, but in the TG exposure there is a lower air flow than in the furnace exposure. This could result in K_2CO_3 not vaporizing completely, which would lead to breaking of the primary protection of the Fe18Cr5Ni sample in the TG exposure but not in the furnace exposure. Another difference of the two exposures is that in the TG exposure the temperature is ramped up to 600 °C, while the furnace exposure starts at 600 °C. The ramping of the temperature contradicts the vaporization of K_2CO_3 as it vaporizes slower at lower temperatures, this observation is however of less significance as the ramping of the temperature takes 6 minutes compared to the 48 hours exposure. When looking at the grain sizes of the alloys it can be noted the mass gain, similarly to the grain size, has a decrease at 5 % nickel. This dip could be explained by that the small grain size results in a faster diffusion of chromium to the oxide and could explain why the primary protection does not break as fast as for the other alloys. However the rest of the grain sizes does not show any similarity to the mass gains.

7
Conclusion

Addition of nickel altered the microstructure of the alloy, as more nickel is added to the alloy it goes from ferrite to austenite. The Fe18Cr5Ni sample showed a duplex behaviour where there were roughly equal amounts of ferrite and austenite grains with a Cr-rich ferritic layer at the top of the alloy. The microstructures did however show some similarity as all of the oxides except for the Fe18Cr5Ni showed split of inward and outward growing oxide. The alloys with 0 weight% and 2 weight% nickel had a near ~60/40 split of inward/outward growing oxide, while the alloys with 10-34 weight% nickel had closer to a ~50/50 split and the alloy with 82 weight% nickel had a ~40/60 split. It is also observed that all the Fe-containing that were tested alloys shows a split of two layers in the outward growing oxide, with exception of the Fe18Cr5Ni which was too thin to analyse.
From the mass gain study from exposures it is shown that adding more than 5 % nickel does not give a significant decrease in mass gain. In the TG exposures for the Fe18Cr10Ni-18Cr82Ni the primary protection breaks immediately which forces the secondary protection to form, which shows that adding more nickel to the alloy is beneficial to a small extent for the secondary protection, as the mass gain is decreased a small amount when the nickel concentration is increased. The results also present that the mass gain is significantly decreased when going from 2 % to 5 % nickel in both exposures, which further strengthens the conclusion that adding nickel is beneficial for the secondary protection.

8

Future works

The SEM images show that there are two layers in most of the outward growing oxides, a TEM analysis would be a good way to confirm the presence of both magnetite and hematite. The TEM would also be used to analyse the cross section of the Fe18Cr5Ni sample. Low incidence angle XRD would be needed to analyze oxides in the nanometer scale and furthermore an XRD analysis of each alloy would be required for an increased understanding of the cross sections.

Alternative methods to prepare the samples such as hot embedding and epoxy casting would be good to minimise the risk of damaging the oxide when the sample is cut. The methods also mitigates the risk of silica deposition during usage of the BIB, with the downside of a small risk to damage the oxide.

It would also be interesting to investigate whether the tube furnace exposures would behave more similar to the TG exposures if the gas flow was reduced to the same flow rate.

Bibliography

[1] NASA earth observatory. Global warming. https://earthobservatory.nasa.gov/features/GlobalWarming/page2.php.

[2] Extreme weather. https://nca2014.globalchange.gov/highlights/report-findings/extreme-weather.

[3] Zeke Hausfather. Analysis: Fossil-fuel emissions in 2018 increasing at fastest rate for seven years. https://bit.ly/2TK4Vps.

[4] J. Lehmusto, B.-J. Skrifvars, P. Yrjas, and M. Hupa. Comparison of potassium chloride and potassium carbonate with respect to their tendency to cause high temperature corrosion of stainless 304l steel. *Fuel Processing Technology*, 105:98 – 105, 2013. Impacts of Fuel Quality on Power Production and Environment.

[5] B. Pujilaksono, T. Jonsson, H. Heidari, M. Halvarsson, J.-E. Svensson, and L.-G. Johansson. Oxidation of binary fecr alloys (fe–2.25cr, fe–10cr, fe–18cr and fe–25cr) in o2 and in o2 + h2o environment at 600 °c. *Oxidation of Metals*, 75(3):183–207, Apr 2011.

[6] Barbara A. Shaw and Robert G. Kelly. What is corrosion? In *INTERFACE*. The Electrochemical Society, 2006.

[7] David J. Young. Chapter 2 - enabling theory. In David J. Young, editor, *High Temperature Oxidation and Corrosion of Metals (Second Edition)*, pages 31 – 84. Elsevier, second edition, 2016.

[8] Per Kofstad. *High temperature corrosion*. Elsevier Applied Science, 1988.

[9] Neil Birks, Gerald H. Meier, and Frederick S. Pettit. *Introduction to the High Temperature Oxidation of Metals*. Cambridge University Press, 2 edition, 2006.

[10] Massachusetts Institute of Technology. Ellingham diagram. http://web.mit.edu/2.813/www/readings/Ellingham_diagrams.pdf.

[11] The National Energy Technology Laboratory of the U.S. Department of Energy. Ellingham diagram. https://www.netl.doe.gov/sites/default/files/event-proceedings/fuel-cells-archive/IC-Pitt-Meier-Extras.pdf.

[12] Johan Eklund. *Material Solutions for Mitigating High Temperature Corrosion in Biomass- and Waste-fired Boilers*. Licentiate thesis, Chalmers University of Technology(CTH), Gothenburg, Sweden, 2018.

[13] Claudia Göbel. *Corrosion of Ferritic Stainless Steels Used in Solid Oxide Fuel Cells*. Licentiate thesis, Chalmers University of Technology(CTH), Gothenburg, Sweden, 2018.

[14] Carl Wagner. Beitrag zur theorie des anlaufvorgangs. *Zeitschrift für Physikalische Chemie*, 21B:25–41, 1933.

[15] Neil Birks, Gerald H. Meier, and Frederick S. Pettit. *Introduction to the High Temperature Oxidation of Metals*. Cambridge University Press, 2 edition, 2006.

[16] Aloke Paul, Tomi Laurila, Vesa Vuorinen, and Sergiy V. Divinski. *Short-Circuit Diffusion*, pages 429–491. Springer International Publishing, Cham, 2014.

[17] Alan Atkinson. Grain-boundary diffusion: an historical perspective. *J. Chem. Soc., Faraday Trans.*, 86:1307–1310, 1990.

[18] Baraa.H.Hadi. Defects in solids: Point defects and line defects. `http://www.uobabylon.edu.iq/eprints/publication_12_10909_1438.pdf`.

[19] James Patterson and Bernard Bailey. *Defects in Solids*, pages 591–612. Springer Berlin Heidelberg, Berlin, Heidelberg, 2010.

[20] Amanda Persdotter. A microstructural investigation of chlorine induced high temperature corrosion of a low alloyed steel. Master thesis, Chalmers University of Technology(CTH), Gothenburg, Sweden, 2016.

[21] M. FROMENT. Foreword. In MICHEL FROMENT, editor, *Passivity of Metals and Semiconductors*, pages IX – X. Elsevier, 1983.

[22] David J. Young. Chapter 3 - oxidation of pure metals. In David J. Young, editor, *High Temperature Oxidation and Corrosion of Metals (Second Edition)*, pages 85 – 144. Elsevier, second edition, 2016.

[23] Eric W. Weisstein. Corundum structure. `http://scienceworld.wolfram.com/chemistry/CorundumStructure.html`.

[24] Eric W. Weisstein. Spinel structure. `http://scienceworld.wolfram.com/chemistry/SpinelStructure.html`.

[25] Gareth S. Parkinsson. Iron oxide surfaces. `https://arxiv.org/ftp/arxiv/papers/1602/1602.06774.pdf`.

[26] E. W. A. Young, P. C. M. Stiphout, and J. H. W de Wit. n-type behavior of chromium (iii) oxide. *Journal of The Electrochemical Society*, pages 884–886, 4 1985.

[27] T. Jonsson, A. Slomian, T. N. Lomholt, S. Kiamehr, and K. V. Dahl. Microstructural investigations of pure nickel exposed to kcl induced high temperature corrosion. *Materials at High Temperatures*, 32(1-2):44–49, 2015.

[28] Penn State University. 8.6: Spinel, perovskite, and rutile structures. `https://bit.ly/2WnFDCZ`.

[29] Joseph I. Goldstein, Dale E. Newbury, Patrick Echlin, David C. Joy, Charles E. Lyman, Eric Lifshin, Linda Sawyer, and Joseph R. Michael. *The SEM and Its Modes of Operation*, pages 21–60. Springer US, Boston, MA, 2003.

[30] Materials Evaluation and Engineering inc. Energy dispersive x-ray spectroscopy (eds). `https://www.mee-inc.com/hamm/energy-dispersive-x-ray-spectroscopyeds/`.

[31] Chalmers University of Technology. Ion-beam techniques. `https://www.chalmers.se/en/researchinfrastructure/CMAL/instruments/FIB/Pages/default.aspx`.

[32] Chalmers University of Technology. Broad ion-beam (bib). `https://www.chalmers.se/en/researchinfrastructure/CMAL/instruments/FIB/BIB/Pages/default.aspx`.

[33] A.K. Chatterjee. 8 - x-ray diffraction. In V.S. Ramachandran and James J. Beaudoin, editors, *Handbook of Analytical Techniques in Concrete Science and Technology*, pages 275 – 332. William Andrew Publishing, Norwich, NY, 2001.

[34] A. W. Coats and J. P. Redfern. Thermogravimetric analysis. a review. *Analyst*, 88:906–924, 1963.

[35] T. Jonsson, S. Karlsson, H. Hooshyar, M. Sattari, J. Liske, J.-E. Svensson, and L.-G. Johansson. Oxidation after breakdown of the chromium-rich scale on stainless steels at high temperature: Internal oxidation. *Oxidation of Metals*, 85(5):509–536, Jun 2016.

A

Appendix 1

A.1 Oxidation thickness calculation

If the mass gain is known and the assumption that the oxide only contains one type of oxide then the following calculations can be used to calculate the thickness of the oxide.

$$\rho_{\text{oxide}} = \frac{\text{m}}{\text{V}} = \frac{\text{m}}{\text{tA}} \tag{A.1}$$

Where ρ is the density of the metal oxide, m is the mass of the oxide and V is the volume of the oxide, which can be rewritten as the thickness, t, of the layer times the surface area, A, of the oxide. As the mass of the oxide can be rewritten to the mass gain that is obtained, equation A.1 can be rewritten as A.2.

$$\text{t} = \frac{\text{W}}{\rho_{\text{recalc}}} \tag{A.2}$$

Where W is the mass gain in mg/cm^2 and the ρ_{recalc} is the density metal oxide times the oxygen molar mass% in the oxide. The calculations for ρ_{recalc} is shown in A.3.

$$\rho_{\text{recalc}} = \text{F} * \rho \tag{A.3}$$

Where F is the molar mass% of oxygen in the metal oxide, which can be calculated with A.4.

$$\text{F} = \frac{\text{M}_{\text{Oxygen in metal oxide}}}{\text{M}_{\text{Metal oxide}}} \tag{A.4}$$

Where M is the molar mass.

A.2 Table of mass gain from the furnace exposures

Table A.1: Average mass gain of each alloy exposed in 5 % O_2 + N_2 + 1 mg/cm^2 K_2CO_3 with its positive and negative standard deviation. The asterisk is from data taken from [27] for the pure nickel and from [5] for the Fe18Cr where the atmosphere was 5 % O_2 40 % H_2O and N_2 and the sample was not sprayed with K_2CO_3.

Test	**Content**	**Average mass gain [mg/cm^2]**	**Positive st.dev [mg/cm^2]**	**Negative st.dev [mg/cm^2]**
1	Fe18Cr*	7.94	-	-
2	Fe18Cr	12.289	0.119	0.142
3	Fe18Cr2Ni	8.424	1.307	1.0167
4	Fe18Cr5Ni	0.569	0.0757	0.143
5	Fe18Cr10Ni	0.886	0.175	0.0947
6	Fe18Cr20Ni	1.253	0.00433	0.00667
7	Fe18Cr34Ni	1.184	0.0727	0.0583
8	18Cr82Ni	0.925	0.0370	0.0270
9	100Ni*	0.830	0.120	0.090